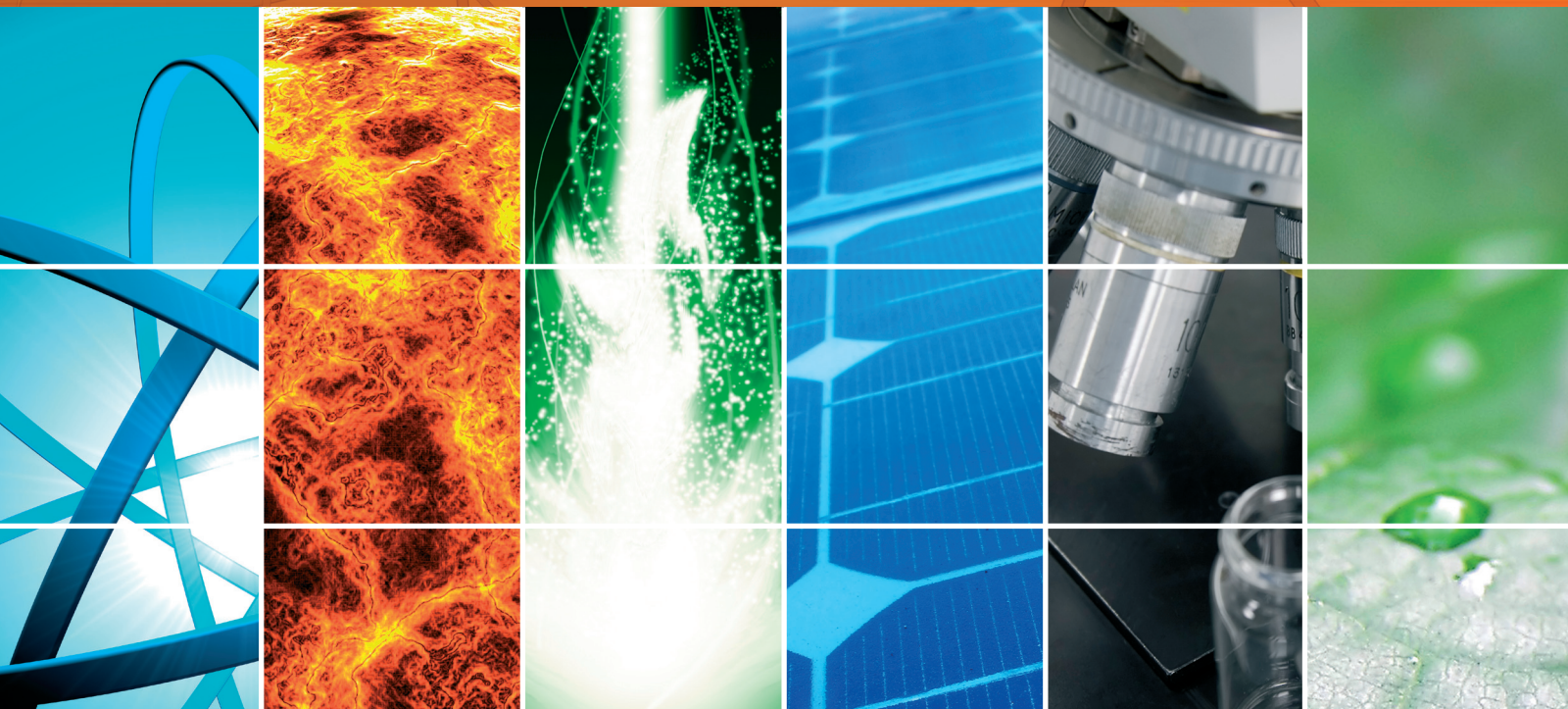


# Organic Electronics

Guest Editors: K. N. Narayanan Unni, Himadri S. Majumdar,  
and Manoj A. G. Nambuthiry





---

# **Organic Electronics**

International Journal of Photoenergy

---

## **Organic Electronics**

Guest Editors: K. N. Narayanan Unni, Himadri S. Majumdar,  
and Manoj A. G. Nambuthiry



---

Copyright © 2013 Hindawi Publishing Corporation. All rights reserved.

This is a special issue published in "International Journal of Photoenergy." All articles are open access articles distributed under the Creative Commons Attribution License, which permits unrestricted use, distribution, and reproduction in any medium, provided the original work is properly cited.

## Editorial Board

M. Sabry Abdel-Mottaleb, Egypt  
Nihal Ahmad, USA  
Nicolas Alonso-Vante, France  
Wayne A. Anderson, USA  
Vincenzo Augugliaro, Italy  
Detlef W. Bahnemann, Germany  
Mohammad A. Behnajady, Iran  
Ignazio Renato Bellobono, Italy  
Raghu N. Bhattacharya, USA  
Pramod H. Borse, India  
Gion Calzaferri, Switzerland  
Adriana G. Casas, Argentina  
Wonyong Choi, Korea  
Věra Cimrova, Czech Republic  
Vikram Dalal, USA  
Dionysios Dionysiou, USA  
Mahmoud M. El-Nahass, Egypt  
Ahmed Ennaoui, Germany  
Chris Ferekides, USA  
Beverley Glass, Australia  
Shinya Higashimoto, Japan  
Yadong Jiang, China  
Chun-Sheng Jiang, USA

Shahed Khan, USA  
Cooper Harold Langford, Canada  
Yuexiang Li, China  
Stefan Lis, Poland  
Niyaz M. Mahmoodi, Iran  
Dionissios Mantzavinos, Greece  
Ugo Mazzucato, Italy  
Jacek Miller, Poland  
Jarugu N. Moorthy, India  
Franca Morazzoni, Italy  
Fabrice Morlet-Savary, France  
Ebinazar B. Namdas, Australia  
Maria da Graça P. Neves, Portugal  
Leonidas Palilis, Greece  
Leonardo Palmisano, Italy  
Ravindra K. Pandey, USA  
David Lee Phillips, Hong Kong  
Pierre Pichat, France  
Gianluca Li Puma, UK  
Xie Quan, China  
Tijana Rajh, USA  
Peter Robertson, UK  
Avigdor Scherz, Israel

Lukas Schmidt-Mende, Germany  
Panagiotis Smirniotis, USA  
Zofia Stasicka, Poland  
Juliusz Sworakowski, Poland  
Nobuyuki Tamaoki, Japan  
Gopal N. Tiwari, India  
Nikolai V. Tkachenko, Finland  
Veronica Vaida, USA  
Roel van De Krol, Germany  
Mark van Der Auweraer, Belgium  
Ezequiel Wolcan, Argentina  
Man Shing Wong, Hong Kong  
David Worrall, UK  
Fahrettin Yakuphanoglu, Turkey  
Minjoong Yoon, Korea  
Hongtao Yu, USA  
Jimmy C. Yu, Hong Kong  
Jun-Ho Yum, Switzerland  
Klaas Zachariasse, Germany  
Lizhi Zhang, China  
Jincai Zhao, China

## Contents

**Organic Electronics**, K. N. Narayanan Unni, Himadri S. Majumdar, and Manoj A. G. Nambuthiry  
Volume 2013, Article ID 364857, 1 page

**Highly Efficient White Organic Light-Emitting Diodes with Controllable Excitons Behavior by a Mixed Interlayer between Fluorescence Blue and Phosphorescence Yellow-Emitting Layers**, Chun-Hong Gao, Xiao-Bo Shi, Dong-Ying Zhou, Lei Zhang, Zhao-Kui Wang, and Liang-Sheng Liao  
Volume 2013, Article ID 831765, 7 pages

**A Novel LTPS-TFT Pixel Circuit to Compensate the Electronic Degradation for Active-Matrix Organic Light-Emitting Diode Displays**, Ching-Lin Fan, Fan-Ping Tseng, Hui-Lung Lai, Bo-Jhang Sun, Kuang-Chi Chao, and Yi-Chiung Chen  
Volume 2013, Article ID 839301, 6 pages

**Optical and Morphological Studies of Thermally Evaporated PTCDI-C8 Thin Films for Organic Solar Cell Applications**, Ronak Rahimi, V. Narang, and D. Korakakis  
Volume 2013, Article ID 205105, 7 pages

**Silver Nanoparticle-Doped Titanium Oxide Thin Films for Intermediate Layers in Organic Tandem Solar Cell**, Wanyi Nie, Robert C. Coffin, and David L. Carroll  
Volume 2013, Article ID 829463, 6 pages

**MEH-PPV and PCBM Solution Concentration Dependence of Inverted-Type Organic Solar Cells Based on Eosin-Y-Coated ZnO Nanorod Arrays**, Riski Titian Ginting, Chi Chin Yap, Muhammad Yahaya, and Muhamad Mat Salleh  
Volume 2013, Article ID 503715, 8 pages

## Editorial

# Organic Electronics

**K. N. Narayanan Unni,<sup>1</sup> Himadri S. Majumdar,<sup>2</sup> and Manoj A. G. Nambuthiry<sup>3</sup>**

<sup>1</sup> CSIR-National Institute for Interdisciplinary Sciences and Technology, Thiruvananthapuram 695 019, India

<sup>2</sup> VTT Technical Research Centre of Finland, Micronova, Tietotie 3, 02150 Espoo, Finland

<sup>3</sup> Indian Institute of Science Education and Research, Thiruvananthapuram 695 016, India

Correspondence should be addressed to K. N. Narayanan Unni; unni@niist.res.in

Received 19 September 2013; Accepted 19 September 2013

Copyright © 2013 K. N. Narayanan Unni et al. This is an open access article distributed under the Creative Commons Attribution License, which permits unrestricted use, distribution, and reproduction in any medium, provided the original work is properly cited.

Although the class of compounds called organic semiconductors was known from early 20th century, it is with the invention of organic light emitting diode (OLED) by Tang and Vanslyke in 1987, the new research area-*organic electronics*-began flourishing. With the progress made in synthetic techniques, purification processes, and fabrication technologies, OLEDs have matured into commercial applications. It is seen that organic photovoltaic (OPV) cells and organic thin film transistors (OTFT) are also following suite. Both polymers and small molecules have been widely studied for possible use in OLEDs, OPV, and OTFT. The prospect of developing flexible and printable electronics on large area makes this field further attractive.

This special issue on Organic Electronics contains 5 research articles which cover organic solar cells, organic light emitting diodes, and back-plane technology for OLED based displays.

Though tandem device structure could be employed to increase the open circuit voltage in organic solar cells, in certain cases this results in charge trapping at the interface and reduced filling factor. W. Nie et al. address this issue by doping the interconnect layer (ZnO) with Ag nanoparticles which results in the mitigation of trapping effect.

In another article, dependence of performance on solution concentration of inverted organic solar cells based on eosin-Y-Coated ZnO nanorod arrays and MEHPPV and PCBM solutions have been studied by R. T. Ginting et al.

R. Rahimi et al. have systematically studied the optical constants, morphology, and structure of thin films of

an important perylene derivative, PTCDI-C8, which will be useful for device design and optimization.

Enhanced charge carrier transport, optimized exciton distribution, and better harvesting of triplets excitons have been obtained by a mixed interlayer in a fluorescent blue-phosphorescent yellow-white OLED by C.-H. Gao et al. A reasonably high efficiency of 29 lumens/watt underlines the importance of this device structure.

The variations in the threshold voltages of driving TFT and the OLED give rise to nonuniform colors in an OLED display. One way of addressing this issue is to deploy more TFTs as part of compensating circuits. The compensation circuit, proposed by C.-L. Fan et al., promises excellent control over the variation in the threshold voltages of TFT and OLED. The circuit contains 5 TFTs and one capacitor. Any improvement in this area with low temperature polycrystalline silicon (LTPS) is important as these problems aggravate as we go to larger and larger displays.

We do believe that these articles not only enrich our knowledge about organic semiconductor devices but also indicate the existence of a lot more technological issues which make the field organic electronics all the more attractive and challenging.

K. N. Narayanan Unni  
Himadri S. Majumdar  
Manoj A. G. Nambuthiry

## Research Article

# Highly Efficient White Organic Light-Emitting Diodes with Controllable Excitons Behavior by a Mixed Interlayer between Fluorescence Blue and Phosphorescence Yellow-Emitting Layers

**Chun-Hong Gao, Xiao-Bo Shi, Dong-Ying Zhou, Lei Zhang, Zhao-Kui Wang, and Liang-Sheng Liao**

*Jiangsu Key Laboratory for Carbon-Based Functional Materials & Devices, Institute of Functional Nano & Soft Materials (FUNSOM), Soochow University, Suzhou, Jiangsu 215123, China*

Correspondence should be addressed to Zhao-Kui Wang; zhaokuiwang@hotmail.com and Liang-Sheng Liao; lsliao@suda.edu.cn

Received 7 January 2013; Revised 18 March 2013; Accepted 19 March 2013

Academic Editor: K. N. Narayanan Unni

Copyright © 2013 Chun-Hong Gao et al. This is an open access article distributed under the Creative Commons Attribution License, which permits unrestricted use, distribution, and reproduction in any medium, provided the original work is properly cited.

A highly efficient hybrid white organic light-emitting diode (HWOLED) has been demonstrated with a mixed interlayer between fluorescent blue and phosphorescent yellow-emitting layers. The device structure is simplified by using a controllable fluorescence-mixed interlayer-phosphorescence emission layer structure. The electroluminescence (EL) performance can be modulated easily by adjusting the ratio of the hole-predominated material to the electron-predominated material in the interlayer. It is found that the HWOLED with a ratio of 3 : 2 exhibits a current efficiency of 34 cd/A and a power efficiency of 29 lm/W at 1000 cd/m<sup>2</sup> with warm white Commission Internationale de l'Éclairage (CIE1931) coordinates of (0.4273, 0.4439). The improved efficiency and adaptive CIE coordinates are attributed to the controllable mixed interlayer with enhanced charge carrier transport, optimized excitons distribution, and improved harvestings of singlet and triplet excitons.

## 1. Introduction

Since firstly reported by Tang and Vanslyke in 1980s [1], organic light-emitting diodes (OLEDs) especially the white OLEDs (WOLEDs) [2] have drawn increasing attention for wide commercial applications in displays and solid-state lighting, owing to their thinness, flexibility, low operation voltage, wide-viewing angle, high resolution, and a fast response time.

Several kinds of structures have been developed for the WOLED fabrications, such as single emitting layer (EML) [3–5], multi EML [6, 7], blue EML with down conversion layer [8], and tandem structures [9–12] employing fluorescent and/or phosphorescent emissive materials. Phosphorescent materials are the outstanding candidates because of their potential for almost 100% internal quantum efficiency [13]. However, few blue phosphorescent materials could be considered as an appropriate candidate for WOLEDs until now owing to their short lifetime and high energy

gap which causes difficulties in keeping color stability and in finding suitable host materials. Hybrid WOLEDs (HWOLEDs) with an architecture of fluorescence blue-interlayer-phosphorescence complementary color (s)-interlayer-fluorescence blue (F-I-P-I-F), proposed by Sun et al. in 2006 [14], have been paid increasing attention due to the long-term stability of fluorescence blue materials and the long lifetime of the color complementary phosphorescent dopants.

The interlayer between fluorescent blue-emitting layer (EML) and complementary phosphorescent EML plays an important role in the efficiency, brightness, and lifetime since it prevents the singlet energy transfer from the blue fluorescent emitter to the complementary phosphorescent emitters and minimizes the exchange energy losses. Various organic materials with hole-predominated property [15–17], electron-predominated property [18], ambipolar properties [19–22], and mixed interlayer (MI) with hole-predominated material and electron-predominated material [23–32] have been used as the interlayer. The MI is a simple way to effectively

balance carrier transporting property to achieve improved EL performance in the devices [25–31]. However, the functions that the ratio of the hole-predominated material to electron-predominated material of MI plays in the location of recombination zone and the harvest mechanism of singlet and triplet excitons are not clear enough. Therefore, systematic investigation in order to achieve a suitable MI is still needed. In this study, we investigate the effects of the ratio of the hole-predominated material to the electron-predominated material in MI on the device efficiency and the white color coordinates in HWOLEDs. In addition, we employed an optimized emitting architecture of fluorescence blue-MI-phosphorescence yellow (F-MI-P) instead of the generally used F-I-P-I-F architecture [14, 20–22] for simplifying the fabrication processes. The blue fluorescence and yellow phosphorescence, instead of conventional doping in the ambipolar host and/or the mixed bipolar property host materials [20–24, 26–28, 30, 31], are doped in the hole-predominated host and the electron-predominated host, respectively.

## 2. Experimental Section

All layers were fabricated on precleaned and 15 min UV-ozone-treated indium-tin-oxide (ITO) electrode on a glass substrate. The thickness and the sheet resistance of the ITO electrode were 110 nm and  $15 \Omega/\square$ , respectively. The organic and metallic layers were subsequently deposited by thermal evaporation under a base pressure of  $2 \times 10^{-6}$  Torr without breaking vacuum. The materials used in this work include molybdenum trioxide ( $\text{MoO}_3$ ) used as both a hole injection material and a *p*-type doping material in hole-transporting layer (HTL). 4,4',4''-Tri(*N*-carbazolyl)triphenylamine (TCTA) is used as both HTL and exciton-blocking layer (EBL). 4,4'-Bis(carbazol-9-yl)biphenyl (CBP) is used as both host and interlayer spacer. 2',2''-(1,3,5-Benzinetriyl)-Tris(1-phenyl-1*H*-benzimidazole) (TPBi) is used as host, interlayer spacer, and electron transport layer (ETL). 4,4'-Bis(9-ethyl-3-carbazovinylene)-1,1'-biphenyl (BCzVBi) is used as a blue fluorescent dopant. Iridium(III)bis(4-phenylthieno[3,2-*c*]pyridinato-*N,C'*)acetylacetonate (PO-01) is used as a yellow phosphorescent dopant. The molecular structures of the organic materials are shown in Figure 1(a). The device structure of the HWOLEDs consists of ITO/ $\text{MoO}_3$  (10 nm)/TcTa :  $\text{MoO}_3$  20 vol.% (65 nm)/TcTa (10 nm)/CBP : BCzVBi 5 vol.% (10 nm)/Spacer (5 nm)/TPBi : PO-01 3 vol.% (20 nm)/TPBi (10 nm)/TPBi : Li 0.8 vol.% (20 nm)/Al (110 nm), where "Spacer" stands for CBP only (Device A), TPBi only (Device B), and CBP : TPBi with varied ratio of 3 : 2 (Device C), 1 : 1 (Device D), and 2 : 3 (Device E), respectively. The lithium-doped TPBi layer [10, 33] is used as both an electron injection layer (EIL) and an electron-transporting layer (ETL). The intrinsic TcTa is used as both an electron-blocking layer (EBL) and an exciton-blocking layer, while 10 nm intrinsic TPBi is used as both a self-hole-blocking layer (HBL) and a self-triplet exciton-blocking layer. The schematic diagram of device structures and the energy diagram is shown in Figure 1(b).

The layer thickness and the deposition rate of the materials were monitored *in situ* using an oscillating quartz thickness monitor. A photometer (Photo Research SpectraScan PR 655) was used to measure the electroluminescent (EL) spectra and Commission Internationale de l'Eclairage (CIE) coordinates of the devices. Combined with a constant current source (Keithley 2400 SourceMeter), the current-voltage characteristic was measured simultaneously. An optical microscope was used to calculate the active area of each device ( $0.1 \text{ cm}^2$ ) for reducing possible device-to-device error.

## 3. Results and Discussion

The interfacial energy barrier between emitting layers is critical to the driving voltage of WOLEDs. The current density-voltage (*J-V*) characteristics shown in Figure 2 exhibit that the driving voltage of HWOLEDs with intrinsic interlayers as spacers (Devices A and B) is higher than that of devices with MIs as spacers (Devices C, D and E) at the same current density. It is reported that a mixed layer of two materials has an intervenient energy level between those of two materials [26, 34]. In the present work, the lowest unoccupied molecular orbital (LUMO) levels of CBP and TPBi are  $-2.5$  and  $-2.8$  eV, and the highest occupied molecular orbital (HOMO) levels of CBP and TPBi are  $-5.9$  and  $-6.3$  eV, respectively. Therefore, the mixed layer of CBP and TPBi is expected to have suitable LUMO and HOMO levels which can reduce interfacial energy barrier for holes and electrons injection in HWOLEDs with MIs.

The ratio of CBP to TPBi in the spacer is critical to the exciton generation interfaces. The EL spectra of the HWOLEDs at  $5 \text{ mA/cm}^2$  in Figure 3 exhibit that the yellow emission intensity is decreasing with the ratio of CBP to TPBi ordered as 1 : 0, 3 : 2, 1 : 1, 2 : 3, and 0 : 1, while the blue emission intensity is increasing with the proportion of CBP decreasing.

Generally, CBP is used as an ambipolar charge transporting material with a predominated-hole-transporting property because its hole mobility ( $2 \times 10^{-3} \text{ cm}^2/\text{V s}$ ) is ten times its electron mobility ( $2 \times 10^{-4} \text{ cm}^2/\text{V s}$ ) [35]. In this work, electrons cannot pass through well because the LUMO of CBP is higher than the LUMO of adjacent TPBi layer. Therefore, in Device A, electrons are blocked from reaching the blue fluorescent EML (BFEML) by a large energy barrier, the main recombination zone of electron and hole is located at the CBP/yellow phosphorescent EML (YPEML) interface, which results in yellow-dominated emission. Whereas, in Device B, the recombination most likely occurs at the BFEML/TPBi interface. The spacer layer prevents the Förster energy transfer from the BFEML to the yellow emitter, while allowing the diffusion of part of the triplets into the YPEML. Therefore, Device B exhibits mainly blue emission. The experimental results demonstrate that MIs act as a role in optimizing the distribution of excitons generated at both BFEML/MI interface and MI/YPEML interface. And the ratio of the yellow emission intensity to the blue emission intensity can be optimized by adjusting the ratio of CBP to TPBi in MIs.

The spacer plays an important role in the singlet and triplet excitons harvesting as well as in the current efficiency

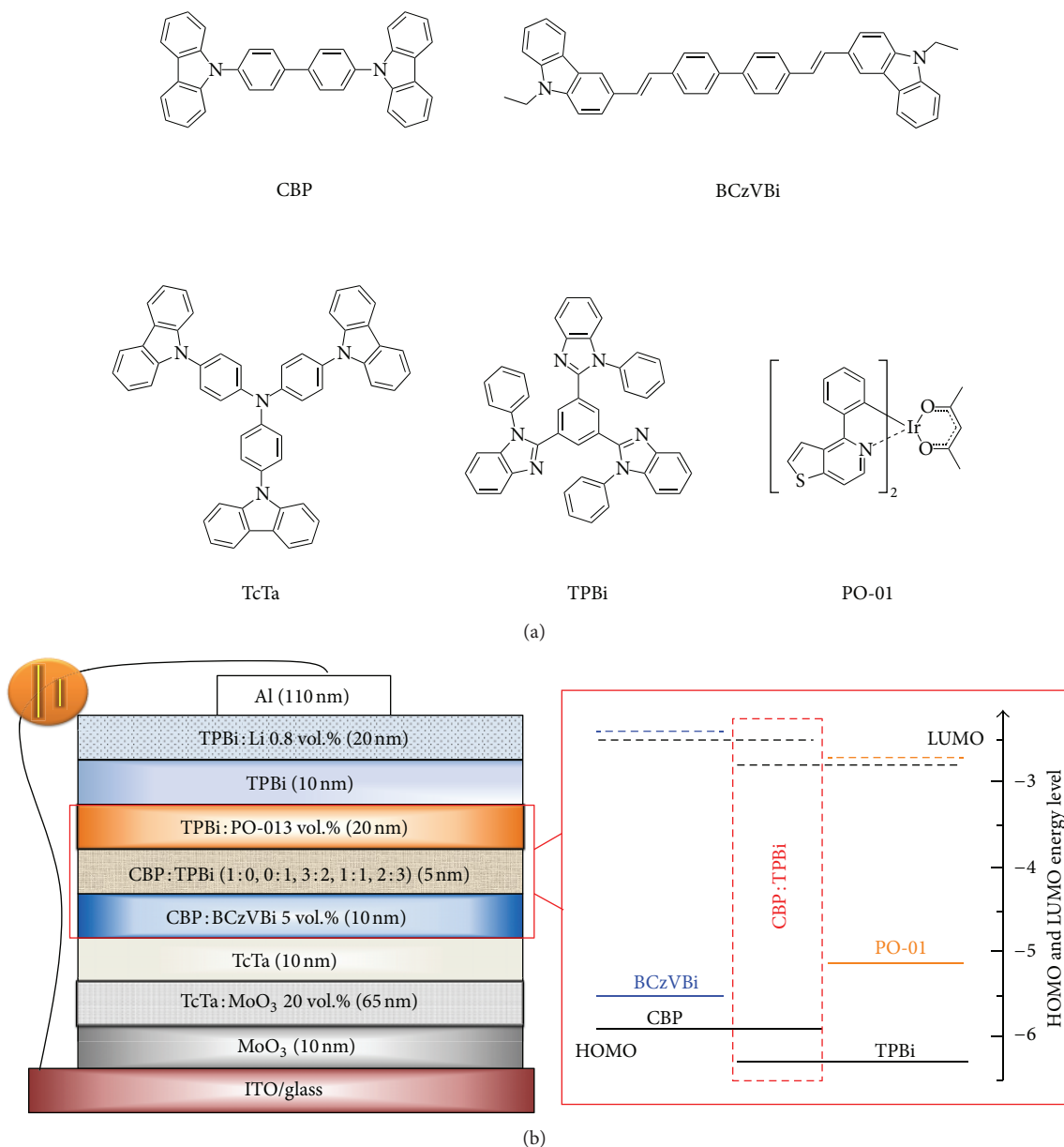


FIGURE 1: (a) The chemical structures of organic materials, (b) the device structure and the energy level diagram of HOMO (solid lines) and LUMO (dashed lines) levels (eV) of HWOLEDs (Devices A, B, C, D, and E). The red dashed box depicts the “Spacer” composed of different ratios of CBP to TPBi.

and power efficiency of HWOLEDs. Figures 4(a) and 4(b) show the relationships of current efficiency and power efficiency of the five HWOLEDs under the same current density, respectively. Device A (with intrinsic CBP as spacer) shows the highest efficiency with a maximum current efficiency of 58.5 cd/A and a maximum power efficiency of 58.8 lm/W at 117 cd/m<sup>2</sup>, and 58.4 cd/A, 51.9 lm/W with CIE coordinate of (0.4907, 0.5015) at 1000 cd/m<sup>2</sup>. Conversely, Device B (with intrinsic TPBi as spacer) shows the lowest efficiency with a current efficiency of 6.98 cd/A and a power efficiency of 6.09 lm/W at 100 cd/m<sup>2</sup>, and 6.43 cd/A, 4.5 lm/W at 1000 cd/m<sup>2</sup>. Furthermore, it demonstrates that both current efficiencies and power efficiencies in the HWOLEDs with

MI spacers are lower than those of Device A and higher than those of Device B, which are strongly dependent on the CBP proportion in MI. The results imply that the harvest of singlet and triplet excitons is crucial in the EL performance. The diffusion length is different for singlet excitons (about several nanometers) and triplet excitons (about several tens of nanometers) [14]. Device A, in which excitons are mainly generated at the CBP/YPEML interface, exhibits the highest efficiency because both singlets and triplets can be harvested by the phosphorescent dopant PO-01, and the triplet Dexter energy transfer from the phosphorescent excitons to the nonradiative triplet state of blue fluorescent emitters is suppressed by the spacer. While Device B, in which excitons

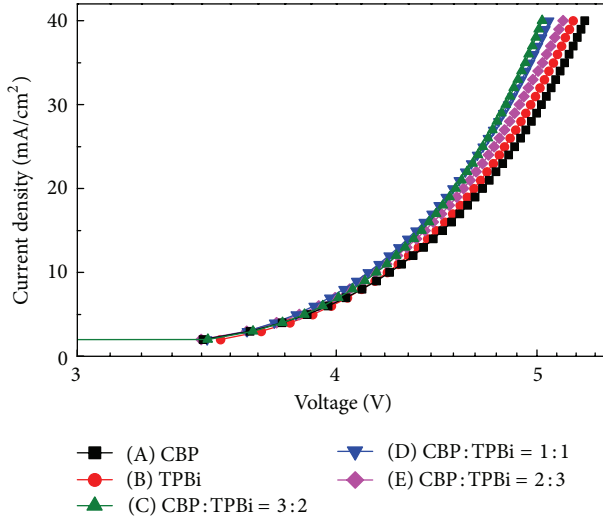


FIGURE 2: The relationship of current density versus voltage in the semilogarithmic scale of HWOLEDs (Devices A, B, C, D, and E).

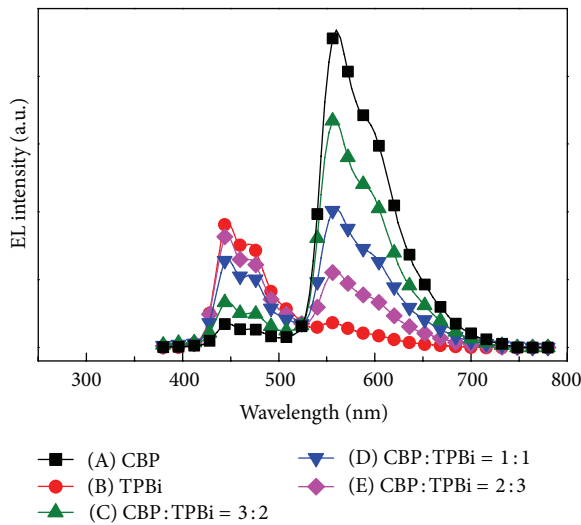


FIGURE 3: The relationship of EL intensity versus wavelength of HWOLEDs (Devices A, B, C, D, and E) at  $5 \text{ mA/cm}^2$ .

are mainly generated at the BFEML/TPBi interface, exhibits the lowest efficiency since the fluorescent dopant BCzVBi can only harvest singlets, and most of the triplets are lost via nonradiative process through the low triplet energy level of BCzVBi. In HWOLEDs with MI, excitons are generated at both the interfaces of BFEML/MI and MI/YPEML. At the interface of BFEML/MI, the generated singlet excitons are harvested by the blue fluorescent dopant (BCzVBi) via Förster energy transfer process, and some of the generated triplet excitons can diffuse into the YPEML and are harvested by the yellow phosphorescent dopant (PO-01) via Dexter energy transfer process. Meanwhile, at the interface of MI/YPEML, the generated singlet excitons and triplet excitons are mainly harvested by the yellow phosphorescent

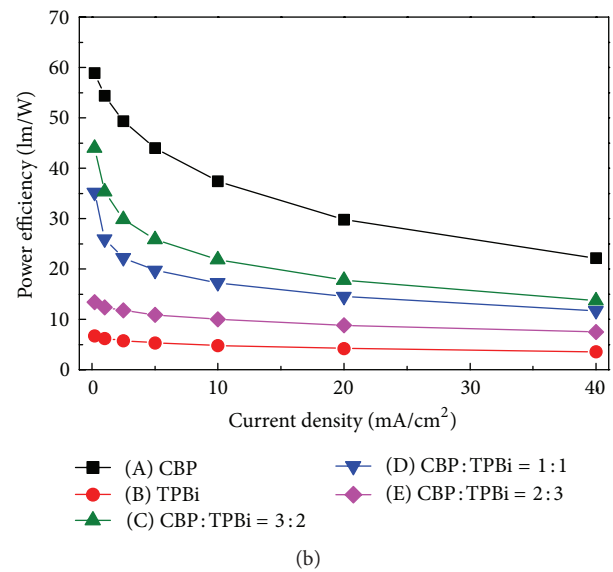
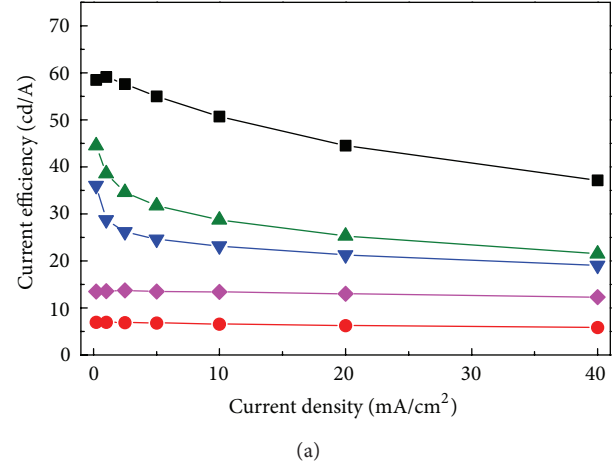


FIGURE 4: The relationships of (a) current efficiency versus current density and (b) power efficiency versus current density of HWOLEDs (Devices A, B, C, D, and E).

dopant (PO-01) via the intersystem crossing process and the Dexter energy transfer process, respectively.

By adjusting the ratio of CBP to TPBi in MI, both the distribution and the harvest of the singlet and triplet excitons are optimized at both BFEML/MI and MI/YPEML interfaces. As a result, Device C (with a ratio of 3:2) achieves a warm white emission with a current efficiency of  $34.1 \text{ cd/A}$  and a maximum power efficiency of  $29 \text{ lm/W}$  at  $1000 \text{ cd/m}^2$  and corresponding CIE coordinate of (0.4273, 0.4439). Particularly, Device D (with a ratio of 1:1) exhibits a warm white emission with a maximum current efficiency of  $36 \text{ cd/A}$  and a maximum power efficiency of  $35.2 \text{ lm/W}$  at  $72 \text{ cd/m}^2$  and corresponding CIE coordinate of (0.4279, 0.4341).

The stability of EL spectra is also one of the key factors to evaluate the performance of WOLEDs. Figures 5(a)–5(e) show the EL spectra, normalized by the main emission peak of PO-01 at 560 nm, for HWOLEDs with different spacers at various current densities. The deep blue emission peak

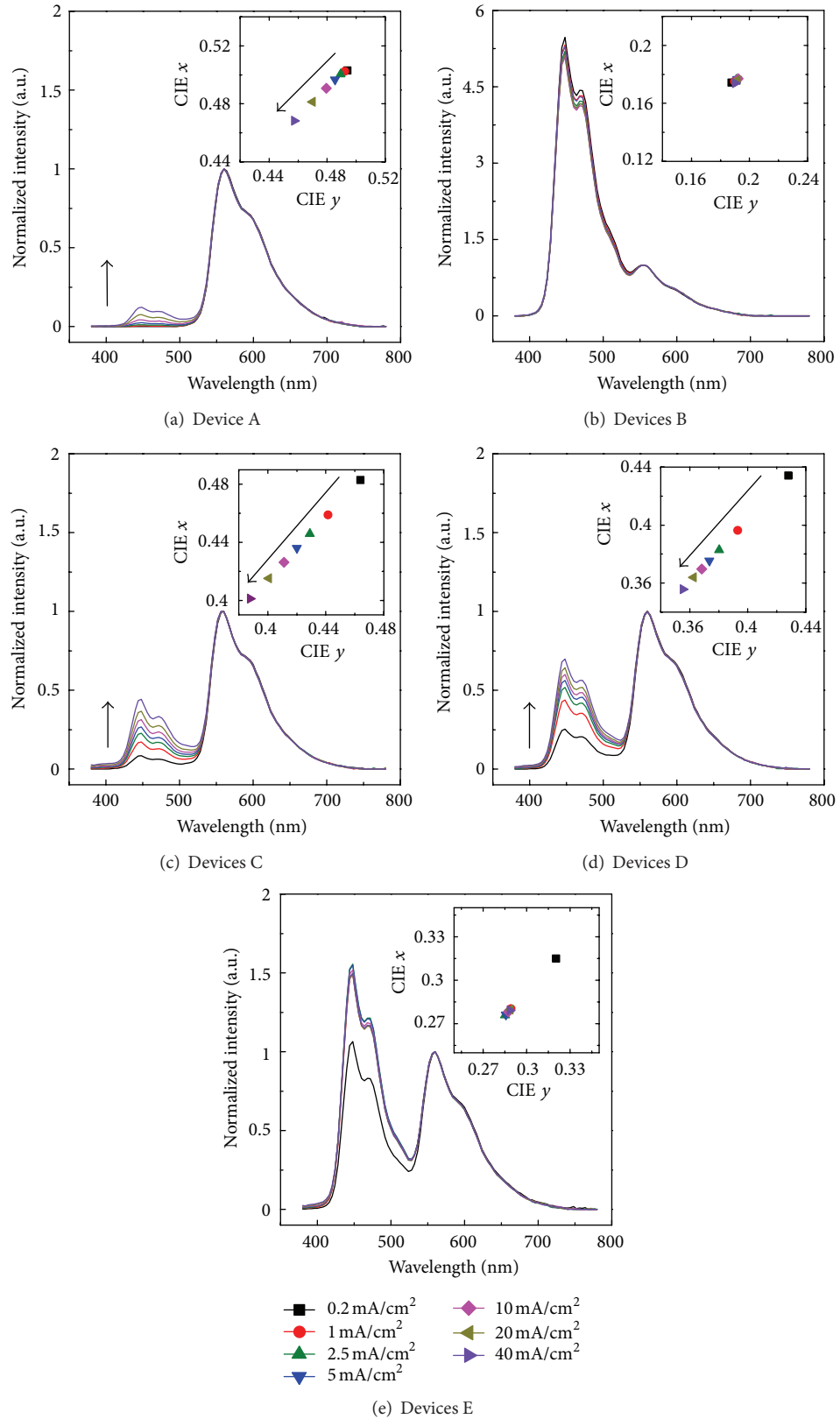


FIGURE 5: (a)–(e) Normalized EL spectra of HWOLEDs with different current density. Each inset shows the corresponding CIE coordinates with the same coordinate scale of  $\Delta$ CIE (0.1, 0.1). The arrows indicate the EL spectral and CIE color coordinates varying with increasing current density from 0.2 to 40 mA/cm<sup>2</sup>.

(~448 nm) in the EL spectra shows three different trends in the five HWOLEDs corresponding to different ratios of CBP : TPBi. With increasing current density, the intensity of deep blue emission peak increases in the devices with high CBP proportion (Devices A (1:0), C (3:2), and D (1:1)), exhibits small changes in the device without CBP doping (Device B (0:1)), and shows a rapid increase firstly and then a small change in the device with low CBP proportion (Device E (2:3)).

With current density increasing, the CIE coordinates exhibit a blue shift in Devices A, C, and D with high CBP proportion. It exhibits a small change of  $\Delta$ CIE (0.002, 0.002) in Device B (0:1), and a  $\Delta$ CIE (0.031, 0.025) shift from 0.2 mA/cm<sup>2</sup> to 1 mA/cm<sup>2</sup> firstly, and then a  $\Delta$ CIE (0.002, 0.002) shift in the subsequent applied current density in Device E. The increased blue emission arises from the ambipolar charge transporting properties of CBP which leads to more electrons injected from TPBi to CBP at an increased current density. As the current density increases, more excitons diffuse to the interface of BFEML/Spacer and cause BCzVBi emission through Förster energy transfer process, resulting in a blue color shift in Devices A, C and D. This indicates that the recombination region is gradually shifted to the interface of BFEML/Spacer interface from Spacer/YPEML interface in the devices with high CBP proportion when increasing the current density. For Device B, the emission zone is located at the interface of BFEML/TPBi and remains unchangeable when increasing the current density. In Device E with low CBP proportion, the emission zone is dominated by CBP at low current density and is located at the interface of Spacer/YPEML. The emission zone is gradually dominated by TPBi with increasing current density and shifts to the interface of BFEML/Spacer interface. However, a HWOLED with a stable EL spectrum can be realized by optimizing the ratio of the hole-predominated material (i.e., CBP) to the electron-predominated material (i.e., TPBi) in MI. In the present work, a cool HWOLED with a stable CIE coordinate of (0.2875 ± 0.002, 0.2782 ± 0.002) is achieved in the luminance range from 136 cd/m<sup>2</sup> to 4916 cd/m<sup>2</sup>.

#### 4. Conclusion

In summary, we have demonstrated a highly efficient warm white OLED with a simplified F-MI-P structure by optimizing the mixing ratio of hole-predominated material (CBP) and electron-predominated material (TPBi) in MI (3:2). The influence of the mixing ratio of the hole-predominated material and the electron-predominated material in MI on the EL performance is investigated. It is found that the improved efficiency with adaptive CIE coordinates is attributed to the enhanced charge carrier transport, optimized excitons distribution at interfaces of both BFEML/MI and MI/YPEML interfaces, and the improved harvest of singlet excitons and triplet excitons, which are modulated by a controllable MI. A cool HWOLED with a stable CIE coordinate off (0.2875 ± 0.002, 0.2782 ± 0.002) is achieved in the luminance range from 136 cd/m<sup>2</sup> to 4916 cd/m<sup>2</sup> with an optimized mixing ratio of CBP : TPBi = 2 : 3 in the MI.

#### Acknowledgments

The authors acknowledge financial support from the Natural Science Foundation of China (nos. 21161160446, 61036009, and 61177016), the National High-Tech Research Development Program (no. 2011AA03A110), the Natural Science Foundation of Jiangsu Province (no. BK2010003). This is also a project funded by the Priority Academic Program Development of Jiangsu Higher Education Institutions (PAPD) and by the Research Supporting Program of Suzhou Industrial Park.

#### References

- [1] C. W. Tang and S. A. Vanslyke, "Organic electroluminescent diodes," *Applied Physics Letters*, vol. 51, no. 12, pp. 913–915, 1987.
- [2] M. C. Gather, A. Kohnen, and K. Meerholz, "White organic light-emitting diodes," *Advanced Materials*, vol. 23, no. 2, pp. 233–248, 2011.
- [3] J. Kido, K. Hongawa, K. Okuyama, and K. Nagai, "White light-emitting organic electroluminescent devices using the poly(N-vinylcarbazole) emitter layer doped with three fluorescent dyes," *Applied Physics Letters*, vol. 64, no. 7, pp. 815–817, 1994.
- [4] Q. Wang, J. Ding, M. Dongge et al., "Harvesting excitons via two parallel channels for efficient white organic LEDs with nearly 100% internal quantum efficiency: fabrication and emission-mechanism analysis," *Advanced Functional Materials*, vol. 19, no. 1, pp. 84–95, 2009.
- [5] J. Ye, C. J. Zheng, X. M. Ou, X. H. Zhang, M. K. Fung, and C. S. Lee, "Management of singlet and triplet excitons in a single emission layer: a simple approach for a high-efficiency fluorescence/phosphorescence hybrid white organic light-emitting device," *Advanced Materials*, vol. 24, no. 25, pp. 3410–3414, 2012.
- [6] J. Kido, M. Kimura, and K. Nagai, "Multilayer white light-emitting organic electroluminescent device," *Science*, vol. 267, no. 5202, pp. 1332–1334, 1995.
- [7] S. Reineke, F. Lindner, G. Schwartz et al., "White organic light-emitting diodes with fluorescent tube efficiency," *Nature*, vol. 459, no. 7244, pp. 234–238, 2009.
- [8] A. R. Duggal, J. J. Shiang, C. M. Heller, and D. F. Foust, "Organic light-emitting devices for illumination quality white light," *Applied Physics Letters*, vol. 80, no. 19, pp. 3470–3472, 2002.
- [9] L. S. Liao, X. F. Ren, W. J. Begley, Y. S. Tyan, and C. A. Pellow, "Tandem white OLEDs combining fluorescent and phosphorescent emission," *SID Symposium Digest of Technical Papers*, vol. 39, no. 1, pp. 818–821, 2008.
- [10] L. S. Liao, K. P. Klubek, and C. W. Tang, "High-efficiency tandem organic light-emitting diodes," *Applied Physics Letters*, vol. 84, no. 2, pp. 167–169, 2004.
- [11] P. Chen, Q. Xue, W. Xie et al., "Color-stable and efficient stacked white organic light-emitting devices comprising blue fluorescent and orange phosphorescent emissive units," *Applied Physics Letters*, vol. 93, no. 15, Article ID 153508, 2008.
- [12] J. P. Yang, Y. Xiao, Y. H. Deng et al., "Electric-field-assisted charge generation and separation process in transition metal oxide-based interconnectors for tandem organic light-emitting diodes," *Advanced Functional Materials*, vol. 22, no. 3, pp. 600–608, 2012.
- [13] M. A. Baldo, D. F. O'Brien, Y. You et al., "Highly efficient phosphorescent emission from organic electroluminescent devices," *Nature*, vol. 395, no. 6698, pp. 151–154, 1998.

- [14] Y. Sun, N. C. Giebink, H. Kanno, B. Ma, M. E. Thompson, and S. R. Forrest, "Management of singlet and triplet excitons for efficient white organic light-emitting devices," *Nature*, vol. 440, no. 7086, pp. 908–912, 2006.
- [15] G. Schwartz, M. Pfeiffer, S. Reineke, K. Walzer, and K. Leo, "Harvesting triplet excitons from fluorescent blue emitters in white organic light-emitting diodes," *Advanced Materials*, vol. 19, no. 21, pp. 3672–3676, 2007.
- [16] G. Schwartz, S. Reineke, T. C. Rosenow, K. Walzer, and K. Leo, "Triplet harvesting in hybrid white organic light-emitting diodes," *Advanced Functional Materials*, vol. 19, no. 9, pp. 1319–1333, 2009.
- [17] Q. Wang, C. L. Ho, Y. Zhao, D. Ma, W. Y. Wong, and L. Wang, "Reduced efficiency roll-off in highly efficient and color-stable hybrid WOLEDs: the influence of triplet transfer and charge-transport behavior on enhancing device performance," *Organic Electronics*, vol. 11, no. 2, pp. 238–246, 2010.
- [18] C. L. Ho, M. F. Lin, W. Y. Wong, W. K. Wong, and C. H. Chen, "High-efficiency and color-stable white organic light-emitting devices based on sky blue electrofluorescence and orange electrophosphorescence," *Applied Physics Letters*, vol. 92, no. 8, Article ID 083301, 2008.
- [19] P. Chen, W. Xie, J. Li et al., "White organic light-emitting devices with a bipolar transport layer between blue fluorescent and orange phosphorescent emitting layers," *Applied Physics Letters*, vol. 91, no. 2, Article ID 023505, 2007.
- [20] J. H. Seo, J. H. Seo, J. H. Park et al., "Highly efficient white organic light-emitting diodes using two emitting materials for three primary colors (red, green, and blue)," *Applied Physics Letters*, vol. 90, no. 20, Article ID 203507, 2007.
- [21] J. H. Seo, J. H. Kim, J. H. Seo et al., "Efficient white organic light-emitting diodes by forming major excitons and preventing T-T annihilation," *SID Symposium Digest of Technical Papers*, p2–38, pp. 1399–1402, 2007.
- [22] P. Chen, L. Zhao, Y. Duan et al., "Efficient white organic light-emitting diodes based on an orange iridium phosphorescent complex," *Journal of Luminescence*, vol. 131, no. 10, pp. 2144–2147, 2011.
- [23] K. S. Yook and J. Y. Lee, "Effect of the interlayer composition on the lifetime and color change of hybrid white organic light-emitting diodes," *Journal of Industrial and Engineering Chemistry*, vol. 17, no. 3, pp. 642–644, 2011.
- [24] K. S. Yook, S. O. Jeon, C. W. Joo, and J. Y. Lee, "Color stability and suppressed efficiency roll-off in white organic light-emitting diodes through management of interlayer and host properties," *Journal of Industrial and Engineering Chemistry*, vol. 15, no. 3, pp. 420–422, 2009.
- [25] G. Schwartz, K. Fehse, M. Pfeiffer, K. Walzer, and K. Leo, "Highly efficient white organic light emitting diodes comprising an interlayer to separate fluorescent and phosphorescent regions," *Applied Physics Letters*, vol. 89, no. 8, Article ID 083509, 2006.
- [26] K. S. Yook, S. O. Jeon, C. W. Joo, and J. Y. Lee, "Low driving voltage in white organic light-emitting diodes using an interfacial energy barrier free multilayer emitting structure," *Journal of Luminescence*, vol. 129, no. 9, pp. 937–940, 2009.
- [27] K. S. Yook, S. O. Jeon, C. W. Joo, and J. Y. Lee, "High efficiency, color stability, and stable efficiency roll off in three color hybrid white organic light emitting diodes," *Applied Physics Letters*, vol. 93, no. 7, Article ID 073302, 2008.
- [28] J. H. Seo, I. H. Park, G. Y. Kim et al., "Hybrid spacer for high-efficiency white organic light-emitting diodes," *Applied Physics Letters*, vol. 92, no. 18, Article ID 183303, 2008.
- [29] G. Schwartz, S. Reineke, K. Walzer, and K. Leo, "Reduced efficiency roll-off in high-efficiency hybrid white organic light-emitting diodes," *Applied Physics Letters*, vol. 92, no. 5, Article ID 053311, 2008.
- [30] J. H. Seo, J. S. Park, S. J. Lee et al., "Codoped spacer ratio effect of hybrid white organic light-emitting diodes," *Current Applied Physics*, vol. 11, no. 3, pp. 564–567, 2011.
- [31] K. S. Yook, S. O. Jeon, J. Y. Lee et al., "High efficiency pure white organic light-emitting diodes using a diphenylaminofluorene-based blue fluorescent material," *Organic Electronics*, vol. 10, no. 7, pp. 1378–1381, 2009.
- [32] F. Zhao, Z. Zhang, Y. Liu, Y. Dai, J. Chen, and D. Ma, "A hybrid white organic light-emitting diode with stable color and reduced efficiency roll-off by using a bipolar charge carrier switch," *Organic Electronics*, vol. 13, no. 6, pp. 1049–1055, 2012.
- [33] L. S. Liao, W. K. Slusarek, T. K. Hatwar, M. L. Ricks, and D. L. Comfort, "Tandem organic light-emitting diode using hexaazatriphenylene hexacarbonitrile in the intermediate connector," *Advanced Materials*, vol. 20, no. 2, pp. 324–329, 2008.
- [34] S. W. Liu, J. H. Lee, C. C. Lee, C. T. Chen, and J. K. Wang, "Charge carrier mobility of mixed-layer organic light-emitting diodes," *Applied Physics Letters*, vol. 91, no. 14, 2007.
- [35] S. Liu, B. Li, L. Zhang, H. Song, and H. Jiang, "Enhanced efficiency and reduced roll-off in nondoped phosphorescent organic light-emitting devices with triplet multiple quantum well structures," *Applied Physics Letters*, vol. 97, no. 8, Article ID 083304, 2010.

## Research Article

# A Novel LTPS-TFT Pixel Circuit to Compensate the Electronic Degradation for Active-Matrix Organic Light-Emitting Diode Displays

Ching-Lin Fan,<sup>1,2</sup> Fan-Ping Tseng,<sup>2</sup> Hui-Lung Lai,<sup>1</sup> Bo-Jhang Sun,<sup>2</sup>  
Kuang-Chi Chao,<sup>1</sup> and Yi-Chiung Chen<sup>2</sup>

<sup>1</sup> Department of Electronic and Computer Engineering, National Taiwan University of Science and Technology, 43 Section 4, Keelung Road, Taipei 106, Taiwan

<sup>2</sup> Graduate Institute of Electro-Optical Engineering, National Taiwan University of Science and Technology, 43 Section 4, Keelung Road, Taipei 106, Taiwan

Correspondence should be addressed to Ching-Lin Fan; [clfan@mail.ntust.edu.tw](mailto:clfan@mail.ntust.edu.tw)

Received 30 January 2013; Accepted 2 April 2013

Academic Editor: K. N. Narayanan Unni

Copyright © 2013 Ching-Lin Fan et al. This is an open access article distributed under the Creative Commons Attribution License, which permits unrestricted use, distribution, and reproduction in any medium, provided the original work is properly cited.

A novel pixel driving circuit for active-matrix organic light-emitting diode (AMOLED) displays with low-temperature polycrystalline-silicon thin-film transistors (LTPS-TFTs) is studied. The proposed compensation pixel circuit is driven by voltage programming scheme, which is composed of five TFTs and one capacitor, and has been certified to provide uniform output current by the Automatic Integrated Circuit Modeling Simulation Program with Integrated Circuit Emphasis (AIM-SPICE) simulator. The results of simulation show excellent performance, such as the low average error rate of OLED current variation ( $<0.5\%$ ) and the low average nonuniformity of OLED current variation ( $<0.8\%$ ) while the shift of threshold voltage of the driving poly-Si TFT and the OLED are both in the worst case ( $\Delta V_{TH} = \pm 0.33$  V for TFT and  $\Delta V_{TH,O} = +0.33$  V for OLED). The proposed pixel circuit shows high immunity to the threshold voltage deviation of both the driving poly-Si TFT and the OLED.

## 1. Introduction

The organic light-emitting diode (OLED) has gained a lot of attention due to its potential advantages, such as light weight, fast response time, wide viewing angle, and high brightness [1–3]. OLED display can be classified into two major driving types: the passive-matrix (PM) driving and active-matrix (AM) driving. The PM driving method has some merits of simple manufacturing process, high yield, and larger aperture ratio. However, it has a challenge of the large size and high-resolution panels because of its high power consumption and short OLED life time [4]. The AM driving uses a thin-film transistor (TFT) backplane to control the gray level of each pixel, achieving lower power consumption and longer OLED life time. Thus, the AM driving method would be a promising candidate to replace the PM driving for higher resolution and larger display sizes.

The low-temperature polycrystalline-silicon (poly-Si) thin-film transistors (LTPS-TFTs) have been widely utilized in active-matrix OLED (AMOLED) displays because of their high current driving capability. However, the LTPS-TFTs have an issue that is the nonuniformity of threshold voltage ( $V_{TH}$ ) and mobility due to process variation, further resulting in different OLED current levels among pixels. In the conventional two-TFT pixel circuit for AMOLED, the various threshold voltages of driving TFT (DTFT) cause nonuniform gray-scale over the display area. Thus, several compensating methods have been developed and can be classified into voltage programming [5–12] and current programming [13–16]. Though the current programming method can compensate for the variation of both mobility and threshold voltage, but it has demerits in that low data current will result in long settling time because of the high parasitic capacitance of data lines. The long settling time is the critical issue for large panels

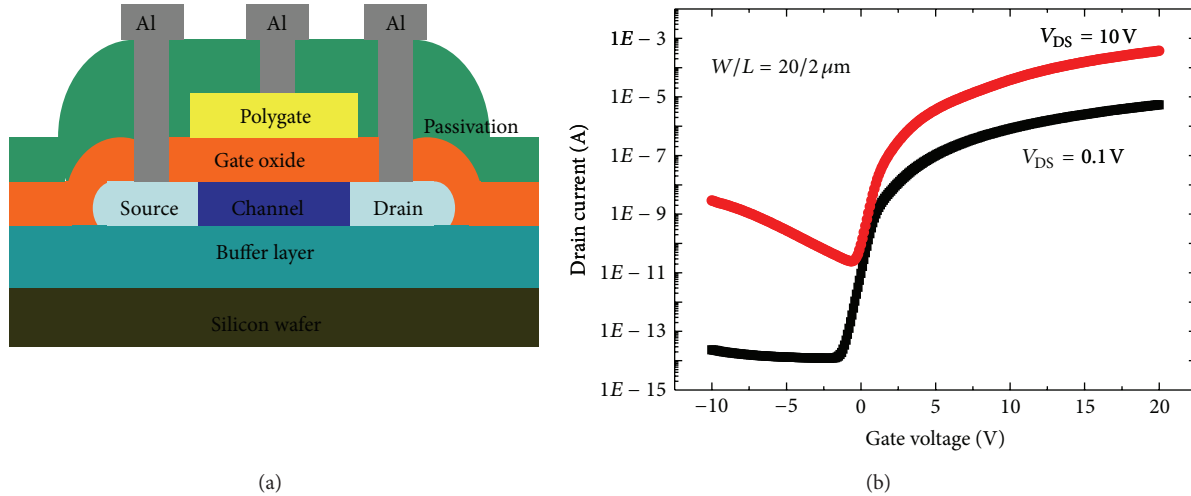


FIGURE 1: (a) Cross-section of the poly-Si TFT. (b) The device transfer curve.

with high resolution. Comparing with current programming method, the voltage programming method is more suitable to be applied in large size and high-resolution panels due to the ability of short settling time.

In addition, since the efficiency and threshold voltage of OLED decays to cause the luminance degradation under a long-time operation [17], many schemes have been reported to compensate for the threshold voltage variation of driving TFT. However, in the published compensated pixel circuits, the number of TFTs, the error rate of OLED current under the TFT threshold voltage deviation, and the degradation of OLED are not usually optimized at the same time [2, 6, 18]. In this study, we propose a new voltage programming AMOLED pixel design. The proposed pixel circuit, which comprised five TFTs and one capacitor (5T1C), has been verified to successfully compensate for the threshold voltage deviation of both the DTFT and the OLED at the same time. And the simulation results demonstrate that the novel design can effectively improve the average error rate ( $<0.5\%$ ) and the nonuniformity ( $<0.8\%$ ) of OLED current. Therefore, the proposed design successfully provides highly stable OLED current and is suitable for large-size and high-resolution displays.

## 2. Process Flow and Poly-Si TFT Characteristics

The poly-Si TFTs were fabricated on silicon wafer. Main features of the LTPS device structure are shown in Figure 1(a). A 110 nm amorphous silicon (a-Si) active layer was deposited on the buffer layer by low-temperature chemical vapor deposition (LPCVD) at  $550^\circ C$ , followed by annealing in nitrogen at  $600^\circ C$ . The poly-Si was patterned for active islands, and a 120 nm thick  $SiO_2$  layer was deposited by plasma-enhanced chemical vapor deposited (PECVD) as a gate insulator. Then, a poly-Si layer was deposited and patterned for gate electrode. The source and drain region were doped with phosphorous ion by the self-aligned ion-implantation at 40 keV to a dose of  $5 \times 10^{15} cm^{-2}$ . The dopants were activated at  $600^\circ C$  for 24

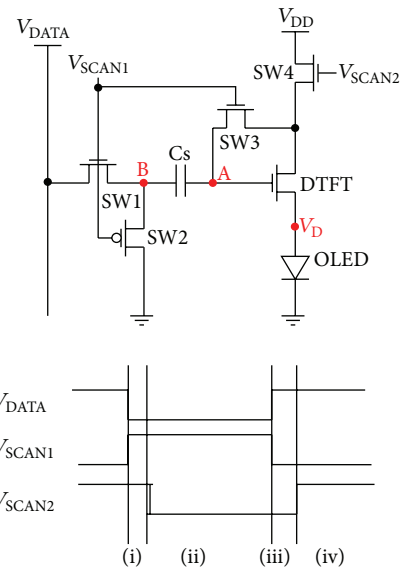


FIGURE 2: Proposed pixel design and timing scheme of the signal line.

hours. Finally, a 500 nm thick PECVD-TEOS oxide was deposited as a passivation layer and patterned for contact holes. Figure 1(b) shows the transfer characteristics of poly-Si TFT with a width of  $20 \mu m$  and length of  $2 \mu m$  at  $V_{DS} = 0.1 V$  and  $V_{DS} = 10 V$ , respectively.

## 3. New Pixel Circuit Design Scheme

As shown in the circuit configuration and timing diagram of Figure 2, the proposed pixel circuit employs five TFTs including four switching TFTs (SW1-SW4), one driving TFT (DTFT), one signal holding capacitor ( $C_s$ ), two scan lines, and one signal data line. The relevant operation stage comprises four states, including precharging, compensating, data input, and emission states. The design parameters of proposed pixel

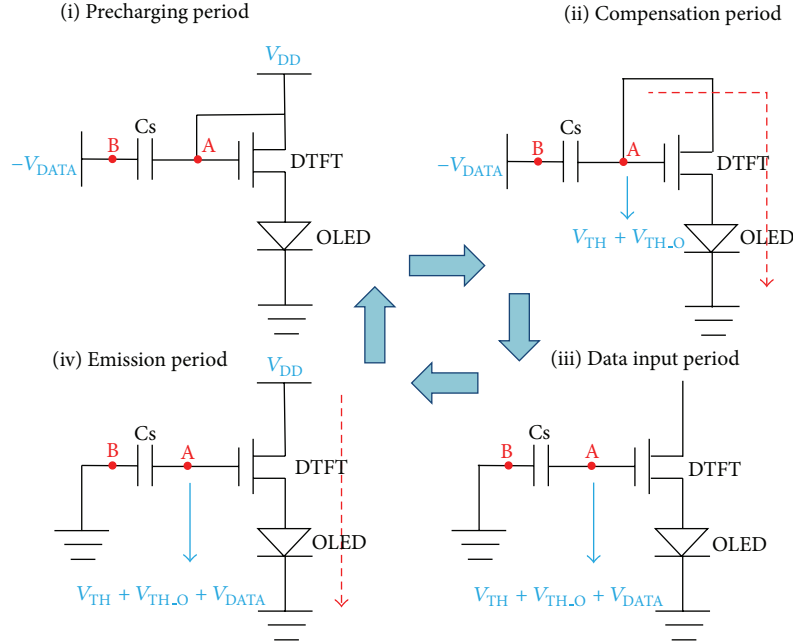


FIGURE 3: Equivalent circuit at each state in operation.

TABLE 1: Simulation parameters of the proposed circuit.

Devices	W/L (SW1–SW4) ( $\mu\text{m}$ )	8/2
	W/L (DTFT) ( $\mu\text{m}$ )	20/2
	$C_s$ (pF)	0.1
	$V_{\text{TH}}$ (DTFT) (V)	1
	$V_{\text{TH},\text{O}}$ (OLED) (V)	1
Signal line	$V_{\text{SCAN1}}$ (V)	-9 to 9
	$V_{\text{SCAN2}}$ (V)	-3 to 15
	$V_{\text{DD}}$ (V)	9
	$V_{\text{DATA}}$ (V)	-5 to -2

circuit are listed in Table 1. As shown in the equivalent operation circuit of Figure 3, the equivalent circuit includes a driving TFT (DTFT) and a signal holding capacitor  $C_s$  in addition to the OLED. It is to be noted that the signal holding capacitor  $C_s$  not only accumulates electric charges from the system power  $V_{\text{DD}}$  but also bleeds/discharges stored electric charges to ground via the DTFT and the OLED, respectively. The operational method and compensation principle of the proposed pixel design are described as follows.

**3.1. Precharging Period.** The task in this period is precharging and resetting the  $V_{\text{DD}} + V_{\text{DATA}}$  stored in the capacitor  $C_s$ . Both  $V_{\text{SCAN1}}$  and  $V_{\text{SCAN2}}$  are high; so, SW1, SW3, and SW4 are turned on, and SW2 is turned off. Therefore, the voltage of the signal holding capacitor  $C_s$  located at node A is charged to approach  $V_{\text{DD}}$  through SW3 and SW4. Furthermore, the data line is biased by a negative voltage. Since the node B is coupled to the data line, the storage voltage across the signal holding capacitor  $C_s$  can be written as  $V_A - V_B = V_{\text{DD}} + V_{\text{DATA}}$ . Hence, the gate voltage of the DTFT connected to the signal

holding capacitor  $C_s$  is also reset for initialization. This stage can get rid of the effects of previous operations.

**3.2. Compensating Period.** In this stage, the threshold voltages of both the DTFT ( $V_{\text{TH}}$ ) and the OLED ( $V_{\text{TH},\text{O}}$ ) are detected by the compensation operation. When  $V_{\text{SCAN1}}$  remains high, it sustains SW1 and SW3 in the “on” state and SW2 in the “off” state. Meanwhile,  $V_{\text{SCAN2}}$  becomes low, and it turns off SW4 only. Hence, the gate voltage of the DTFT continues discharging through SW3, DTFT, and OLED until the DTFT is turned off. In this way, the gate voltage of the DTFT that has a diode-connect structure will reach  $V_{\text{TH}} + V_{\text{TH},\text{O}}$ , where  $V_{\text{TH}}$  is the threshold voltage of the DTFT, and  $V_{\text{TH},\text{O}}$  is the threshold voltage of the OLED.

**3.3. Data Input Period.** In the data input stage, when  $V_{\text{SCAN1}}$  returns to a low value, it turns off SW1 and SW3 and turns on SW2 simultaneously. At this moment,  $V_{\text{SCAN2}}$  constantly remains low, which forces SW4 in the “off” state. Furthermore, voltage at node B is applied by zero voltage. Thus, the voltage at node B of the signal holding capacitor  $C_s$  becomes zero voltage, and the gate of DTFT is charged up to a high potential, which is high enough not to interfere with the compensation operation at the next frame. The gate voltage of the DTFT is boosted up to  $V_{\text{TH}} + V_{\text{TH},\text{O}} + V_{\text{DATA}}$  by the conservation of charge in the capacitor  $C_s$ .

**3.4. Emission Period.** In the emission stage, when  $V_{\text{SCAN1}}$  continues low, it keeps both SW1 and SW3 in the “off” state and keeps SW2 in the “on” state. Meanwhile,  $V_{\text{SCAN2}}$  becomes high; as a result, it turns on SW4. In addition, the node B is continuously applied by zero voltage. Hence, the signal holding capacitor  $C_s$  maintains the gate voltage of the DTFT, as

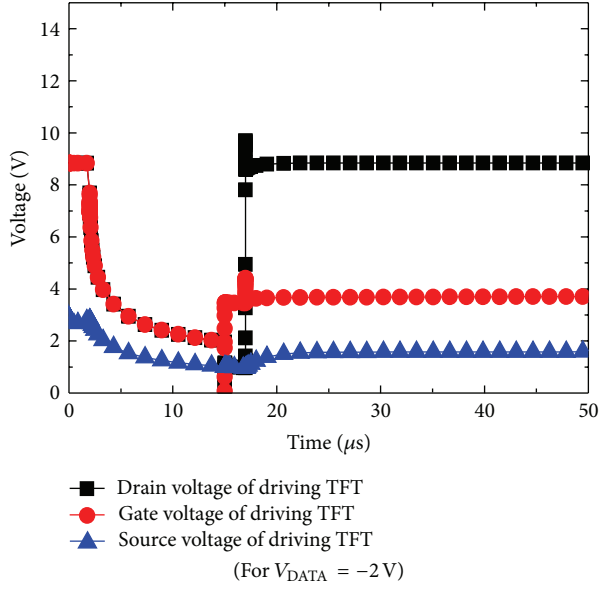


FIGURE 4: Gate, source, and drain voltage of DTFT with operation stages when  $V_{DATA} = -2$  V.

mentioned earlier, up to the next cycle of precharging stage. The OLED current ( $I_{OLED}$ ) can be written using the drain current of the DTFT in the saturation region as

$$\begin{aligned} I_{OLED} &= \frac{1}{2} K_{DTFT} (V_{GS_{DTFT}} - V_{TH})^2 \\ &= \frac{1}{2} K_{DTFT} (V_{TH} + V_{TH,0} + |V_{DATA}| - V_D - V_{TH})^2 \quad (1) \\ &= \frac{1}{2} K_{DTFT} (|V_{DATA}| + V_{TH,0} - V_D)^2, \end{aligned}$$

where  $V_D$  is the anode voltage of OLED when OLED is emitting. Therefore,  $I_{OLED}$  is independent of the threshold voltage deviation of DTFT, and only affected by  $V_{DATA}$ ,  $V_{TH,0}$ , and  $V_D$ . The threshold voltage of OLED ( $V_{TH,0}$ ) will be increased when the OLED degrades under long time operation, so that the OLED driving current is also increased to compensate for the degraded luminance of OLED during the emitting period. Thus, we believe that the proposed pixel circuit can also compensate the threshold voltage degradation of OLED and DTFT under the long operation time at the same time.

#### 4. Result and Discussion

In this study, we had used poly-Si TFT model of AIM-SPICE with level 16 for pixel circuit simulation. And the OLED was modeled by a diode-connected poly-Si TFT and a capacitor. The OLED capacitance was set to 25 nF/cm<sup>2</sup> in this simulation. And the dimension of the channel width/length for DTFT had been set to 20/2 μm.

The gate, drain, and source node's voltages of DTFT under the data voltage  $V_{DATA}$  (-2 V) are shown in Figure 4. At the end of compensating period, the gate voltage of DTFT is discharged until 2 V ( $V_{TH} + V_{TH,0}$ ), where  $V_{TH}$  is the threshold

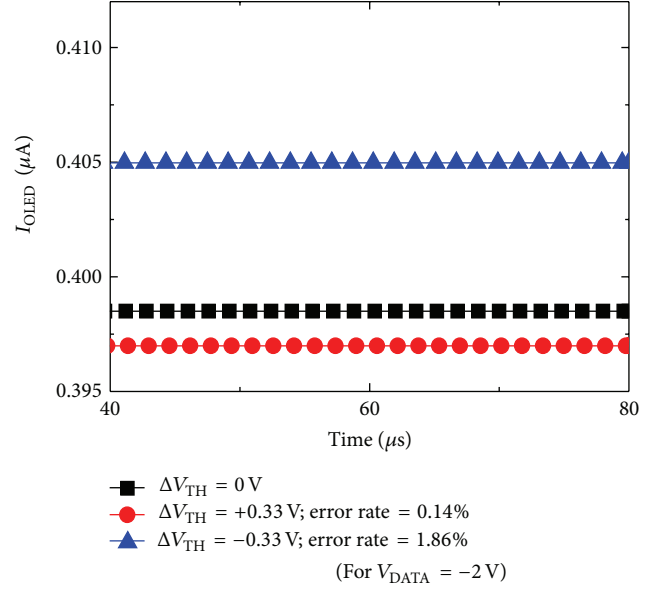


FIGURE 5: The OLED current with the variation in the threshold voltage of DTFT when  $V_{DATA} = -2$  V.

voltage of DTFT, and  $V_{TH,0}$  is the threshold voltage of OLED. The expectancy of circuit operation is verified by the simulation result. During the emission period, the gate voltage of DTFT is 4 V ( $V_{TH} + V_{TH,0} + |V_{DATA}|$ ). Thus, the  $V_{GS}$  of DTFT is  $V_{TH} + V_{TH,0} + |V_{DATA}| - V_D$ , where  $V_D$  is the voltage of OLED when OLED is emitting light. Thus, the proposed pixel circuit can efficiently compensate for the OLED degradation.

The OLED current with the threshold voltage deviation of DTFT ( $\Delta V_{TH} = \pm 0.33$  V) under the data voltage (-2 V) is shown in Figure 5. The error rate of the OLED current is defined as the difference between the shifted OLED current of driving TFT ( $\Delta V_{TH} = \pm 0.33$  V) and the normal OLED current ( $\Delta V_{TH} = 0$  V), as follows:

$$\text{error rate} = \frac{I_{OLED}(\Delta V_{TH} = \pm 0.33 \text{ V}) - I_{OLED}(\Delta V_{TH} = 0 \text{ V})}{I_{OLED}(\Delta V_{TH} = 0 \text{ V})} \quad (2)$$

It is found that the error rates of the OLED current under the  $\Delta V_{TH} = \pm 0.33$  V of DTFT for input  $V_{DATA} = -2$  V were 0.14% and 1.86%, respectively. The driving current of OLED will affect the luminance of OLED and thus represent the display brightness because the OLED is current driving unit. The simulation result has shown that the current variation of OLED caused by the threshold voltage deviation of DTFT is very small. Figure 6 shows the error rates of OLED current at different data voltages ( $|V_{DATA}|$ ) with the threshold voltage deviation of DTFT ( $\Delta V_{TH} = \pm 0.33$  V). The error rate of OLED current is the deviation percentage of the original OLED current ( $\Delta V_{TH} = 0$  V) when the varied threshold voltage of DTFT is +0.33 or -0.33 V. It can be clearly showed that the maximum error rate of OLED current is below 2%, and the average error rate is 0.5% for the proposed pixel circuit. In the conventional 2T1C pixel circuit, the average error rate

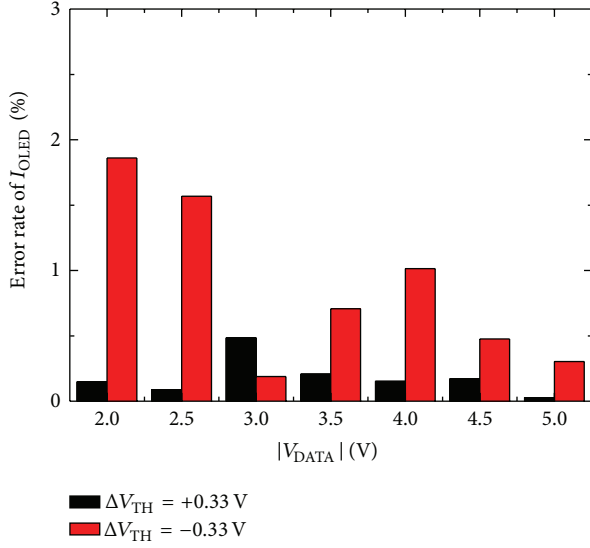


FIGURE 6: The error rates of  $I_{OLED}$  at different  $V_{DATA}$  with threshold voltage variations ( $\Delta V_{TH} = -0.33$  and  $+0.33$  V); the average error rate is 0.5%.

is about 30%. Therefore, the display image quality of the proposed pixel circuit will be more uniform than that in the other reports [12]. The results can prove that the proposed pixel circuit has high immunity to the threshold voltage deviation of DTFT. As a result, the proposed pixel circuit is capable of providing a uniform OLED driving current regardless of the variation in the poly-Si TFT performance.

The increases in OLED threshold voltage ( $V_{TH,O}$ ) with emission for a long time degrade the display image quality. Figure 7 shows the nonuniformity of OLED current in the worst case ( $\Delta V_{TH} = \pm 0.33$  V and  $\Delta V_{TH,O} = +0.33$  V) for different data voltages ( $|V_{DATA}|$ ) for the proposed pixel circuit and the conventional 2T1C pixel circuit, respectively. The  $I_{OLED}$  nonuniformity is defined as the difference between the maximum OLED current ( $I_{OLEDMAX}$  when  $\Delta V_{TH} = -0.33$  V for TFT,  $\Delta V_{TH,O} = 0$  for OLED) and the minimum OLED current ( $I_{OLEDMIN}$  when  $\Delta V_{TH} = +0.33$  V for TFT,  $\Delta V_{TH,O} = +0.33$  for OLED), divided by their average OLED current ( $(I_{OLEDMAX} + I_{OLEDMIN})/2$ ) as follows:

$$\text{nonuniformity} = \frac{I_{OLEDMAX} (\Delta V_{TH} = -0.33 \text{ V}, \Delta V_{TH,O} = 0)}{(I_{OLEDMAX} + I_{OLEDMIN})/2} - \frac{I_{OLEDMIN} (\Delta V_{TH} = +0.33 \text{ V}, \Delta V_{TH,O} = +0.33)}{(I_{OLEDMAX} + I_{OLEDMIN})/2}. \quad (3)$$

The uniformity of display image can be improved by reducing the nonuniformity of OLED current. Compared with simulation results for the conventional 2T1C pixel circuit and the reported compensating circuit [19], the proposed circuit can offer a more stable driving current, which is independent of the threshold voltage variation of DTFT ( $\Delta V_{TH} = \pm 0.33$  V) and the degraded OLED threshold voltage

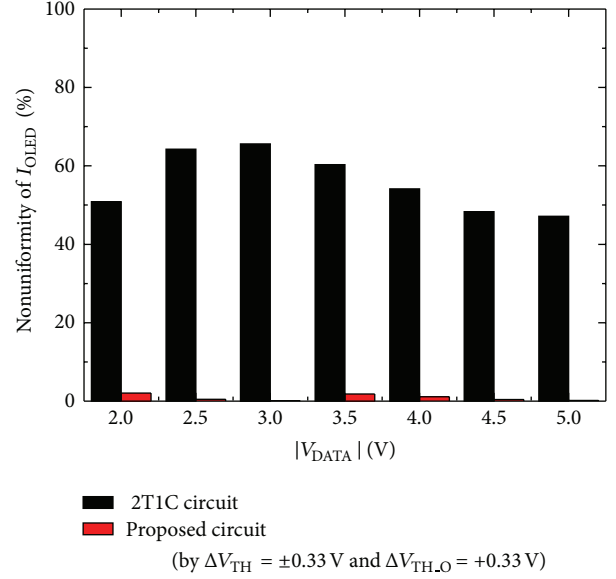


FIGURE 7: The nonuniformity of  $I_{OLED}$  at different  $V_{DATA}$  under the worst case ( $\Delta V_{TH} = \pm 0.33$  V and  $\Delta V_{TH,O} = +0.33$  V). The average nonuniformity is 0.89%.

( $\Delta V_{TH,O} = +0.33$  V) for different data voltages. For the proposed pixel circuit, the average nonuniformity is approximately 0.89%. In addition, the average nonuniformity of the conventional 2T1C pixel circuit and the reported compensating circuit (5T2C) is about 55% and 5.7%, respectively [19]. Clearly, the proposed pixel circuit has high immunity to DTFT threshold voltage shifts and OLED degradation, resulting from the compensation for the threshold voltage deviation of DTFT and OLED aging phenomenon at the same time.

## 5. Conclusion

A novel voltage programming pixel circuit for active-matrix organic light-emitting diode (AMOLED) displays was studied. The proposed circuit was verified by AIM-SPICE simulator. The proposed circuit consisted of five TFTs and one capacitor and successfully compensated for the threshold voltage deviation of DTFT and the degradation of OLED. The average nonuniformity of the proposed pixel circuit is approximately 0.8% in the worst case. The proposed pixel circuit design can provide stable driving current to the AMOLED panel for achieving high-resolution images, thereby promising candidate for the large size and high-resolution AMOLED panels.

## Acknowledgment

The authors would like to acknowledge the financial support from the National Science Council (NSC) under Contract nos. NSC-100-2221-E-011-141 and NSC 99-2221-E011-137.

## References

- [1] C. Hosokawa, M. Matsuura, M. Eida, K. Fukuoka, H. Tokailin, and T. Kusumoto, "Full-color organic EL display," *Journal of*

- the Society for Information Display*, vol. 6, no. 4, pp. 257–260, 1998.
- [2] C. W. Lin, D. Z. Pang, R. Lee et al., “Advanced poly-Si device and circuitry for AMOLED and high-integration AMLCD,” in *Proceedings of the International Display Manufacturing Conference and Exhibition (IDMC '05)*, pp. 315–318, February 2005.
  - [3] M. A. Dawson, Z. Shen, D. A. Furst et al., “The impact of the transient response of organic light emitting diodes on the design of active matrix OLED displays,” in *Proceedings of IEEE International Electron Device Meeting (IEDM '98)*, pp. 875–878, December 1998.
  - [4] M. Kimura, I. Yudasaka, S. Kanbe et al., “Low-temperature polysilicon thin-film transistor driving with integrated driver for high-resolution light emitting polymer display,” *IEEE Transactions on Electron Devices*, vol. 46, no. 12, pp. 2282–2288, 1999.
  - [5] J. H. Lee, B. H. You, W. J. Nam, H. J. Lee, and M. K. Han, “A new a-Si:H TFT pixel design compensating threshold voltage degradation of TFT and OLED,” *SID Symposium Digest of Technical Papers*, vol. 35, no. 1, pp. 264–267, 2004.
  - [6] S. M. Choi, O. K. Kwon, and H. K. Chung, “An improved voltage programmed pixel structure for large size and high resolution AM-OLED displays,” *SID Symposium Digest of Technical Papers*, vol. 35, no. 1, pp. 260–263, 2004.
  - [7] H. Y. Lu, P. T. Liu, T. C. Chang, and S. Chi, “Enhancement of brightness uniformity by a new voltage-modulated pixel design for AMOLED displays,” *IEEE Electron Device Letters*, vol. 27, no. 9, pp. 743–745, 2006.
  - [8] J. H. Lee, S. G. Park, J. H. Jeon et al., “New fraction time annealing method for improving organic light emitting diode current stability of hydrogenated amorphous silicon thin-film transistor based active matrix organic light emitting diode backplane,” *Japanese Journal of Applied Physics*, vol. 46, no. 3, pp. 1350–1353, 2007.
  - [9] H. S. Shin, W. K. Lee, S. G. Park, S. H. Kuk, and M. K. Han, “Active-matrix organic light emission diode pixel circuit for suppressing and compensating for the threshold voltage degradation of hydrogenated amorphous silicon thin film transistors,” *Japanese Journal of Applied Physics*, vol. 48, no. 3, Article ID 03B023, 4 pages, 2009.
  - [10] C. L. Fan, Y. S. Lin, and Y. W. Liu, “Low temperature polycrystalline silicon thin film transistor pixel circuits for active matrix organic light emitting diodes,” *IEICE Transactions on Electronics*, vol. 93, no. 5, pp. 712–714, 2010.
  - [11] C. L. Fan, Y. Y. Lin, B. S. Lin, J. Y. Chang, and H. C. Chang, “New pixel circuit compensating poly-si TFT threshold-voltage shift for a driving AMOLED,” *Journal of the Korean Physical Society*, vol. 56, no. 4, pp. 1185–1189, 2010.
  - [12] C. L. Fan, Y. Y. Lin, J. Y. Chang, B. J. Sun, and Y. W. Liu, “A new low temperature polycrystalline silicon thin film transistor pixel circuit for active matrix organic light emitting diode,” *Japanese Journal of Applied Physics*, vol. 49, no. 6, Article ID 064201, 5 pages, 2010.
  - [13] J. H. Lee, W. J. Nam, S. H. Jung, and M. K. Han, “A new current scaling pixel circuit for AMOLED,” *IEEE Electron Device Letters*, vol. 25, no. 5, pp. 280–282, 2004.
  - [14] Y. He, R. Hattori, and J. Kanicki, “Four-thin film transistor pixel electrode circuits for active-matrix organic light-emitting displays,” *Japanese Journal of Applied Physics*, vol. 40, pp. 1199–1208, 2001.
  - [15] J. H. Lee, W. J. Nam, C. Y. Kim, H. S. Shin, C. D. Kim, and M. K. Han, “New current-scaling pixel circuit compensating non uniform electrical characteristics for active matrix organic light emitting diode,” *Japanese Journal of Applied Physics*, vol. 45, pp. 4402–4406, 2006.
  - [16] H. Lee, J. S. Yoo, C. D. Kim, I. J. Chung, and J. Kanicki, “Novel current-scaling current-mirror hydrogenated amorphous silicon thin-film transistor pixel electrode circuit with cascade capacitor for active-matrix organic light-emitting devices,” *Japanese Journal of Applied Physics*, vol. 46, no. 3, pp. 1343–1349, 2007.
  - [17] C. L. Lin, W. Y. Chang, C. C. Hung, and C. D. Tu, “LTPS-TFT pixel circuit to compensate for OLED luminance degradation in three-dimensional AMOLED display,” *IEEE Electron Device Letters*, vol. 33, no. 5, pp. 700–702, 2012.
  - [18] B. T. Chen, Y. H. Tai, Y. J. Kuo, C. C. Tsai, and H. C. Cheng, “New pixel circuits for driving active matrix organic light emitting diodes,” *Solid-State Electronics*, vol. 50, no. 2, pp. 272–275, 2006.
  - [19] W. J. Wu, L. Zhou, R. H. Yao, and J. B. Peng, “A new voltage-programmed pixel circuit for enhancing the uniformity of AMOLED displays,” *IEEE Electron Device Letters*, vol. 32, no. 7, pp. 931–933, 2011.

## Research Article

# Optical and Morphological Studies of Thermally Evaporated PTCDI-C8 Thin Films for Organic Solar Cell Applications

Ronak Rahimi,<sup>1</sup> V. Narang,<sup>2</sup> and D. Korakakis<sup>1</sup>

<sup>1</sup> Lane Department of Computer Science and Electrical Engineering, West Virginia University, Morgantown, WV 26506, USA

<sup>2</sup> Department of Physics, West Virginia University, Morgantown, WV 26506, USA

Correspondence should be addressed to Ronak Rahimi; rrahimi@mix.wvu.edu

Received 28 November 2012; Accepted 25 February 2013

Academic Editor: Himadri S. Majumdar

Copyright © 2013 Ronak Rahimi et al. This is an open access article distributed under the Creative Commons Attribution License, which permits unrestricted use, distribution, and reproduction in any medium, provided the original work is properly cited.

PTCDI-C8 due to its relatively high photosensitivity and high electron mobility has attracted much attention in organic semiconductor devices. In this work, thin films of PTCDI-C8 with different thicknesses were deposited on silicon substrates with native silicon dioxide using a vacuum thermal evaporator. Several material characterization techniques have been utilized to evaluate the structure, morphology, and optical properties of these films. Their optical constants (refractive index and extinction coefficient) have been extracted from the spectroscopic ellipsometry (SE). X-ray reflectivity (XRR) and atomic force microscopy (AFM) were employed to determine the morphology and structure as well as the thickness and roughness of the PTCDI-C8 thin films. These films revealed a high degree of structural ordering within the layers. All the experimental measurements were performed under ambient conditions. PTCDI-C8 films have shown to endure ambient condition which allows *post-deposition* characterization.

## 1. Introduction

Small organic molecules represent a remarkable group of materials that exhibit alterable physical, optical, and electrical properties. Furthermore, charge transport and optical properties of organic thin films are strongly dependent on the overlap between the molecular orbitals of the neighboring molecules [1]. Hence, determination of the molecular packing of the organic thin films is an essential input for a comprehensive understanding of the correlation between the material structure and the device optical and electrical properties. Perylene Tetracarboxylic Diimide derivatives are among the most promising small organic molecules to fabricate organic thin film transistors (OTFTs) and organic solar cells (OSCs) [2–5]. Their optical and electrical properties can be modified by attaching different functional groups at specific molecular positions [6, 7]. PTCDI-C8 (N,N'-Dioctyl-3,4,9,10 perylenedicarboximide) is a compound belonging to the perylenes family that shows high photosensitivity (~20%) [8] and high electron mobility (~0.6–1.7 cm<sup>2</sup>/Vs) [9, 10]. Since structural properties of thin films are defining parameters of the device optical and electrical characteristics,

a detailed study of the morphological properties of PTCDI-C8 thin films is essential to optimize the performance of the devices based on this material. Although investigation of the structure of the PTCDI-C8 on different substrates has been reported before [11], the importance of the material effects on the device performance is the main reason for the continuing research in this area. In this work, optical properties and molecular structure of PTCDI-C8 thin films have been investigated combining several material characterization techniques such as ellipsometry, AFM, and XRR. The obtained results revealed a high degree of structural ordering that explains the superior electrical and optical properties of these films.

## 2. Experimental

Several sets of PTCDI-C8 films with thicknesses ranging from 20 to 45 nm were deposited on p-type boron-doped Si (111) substrates with native oxide using a vacuum thermal evaporator system. These films were deposited under high vacuum condition with a base pressure of about  $4 \times 10^{-7}$  Torr at a rate of 1 Å/sec at room temperature. Topographic

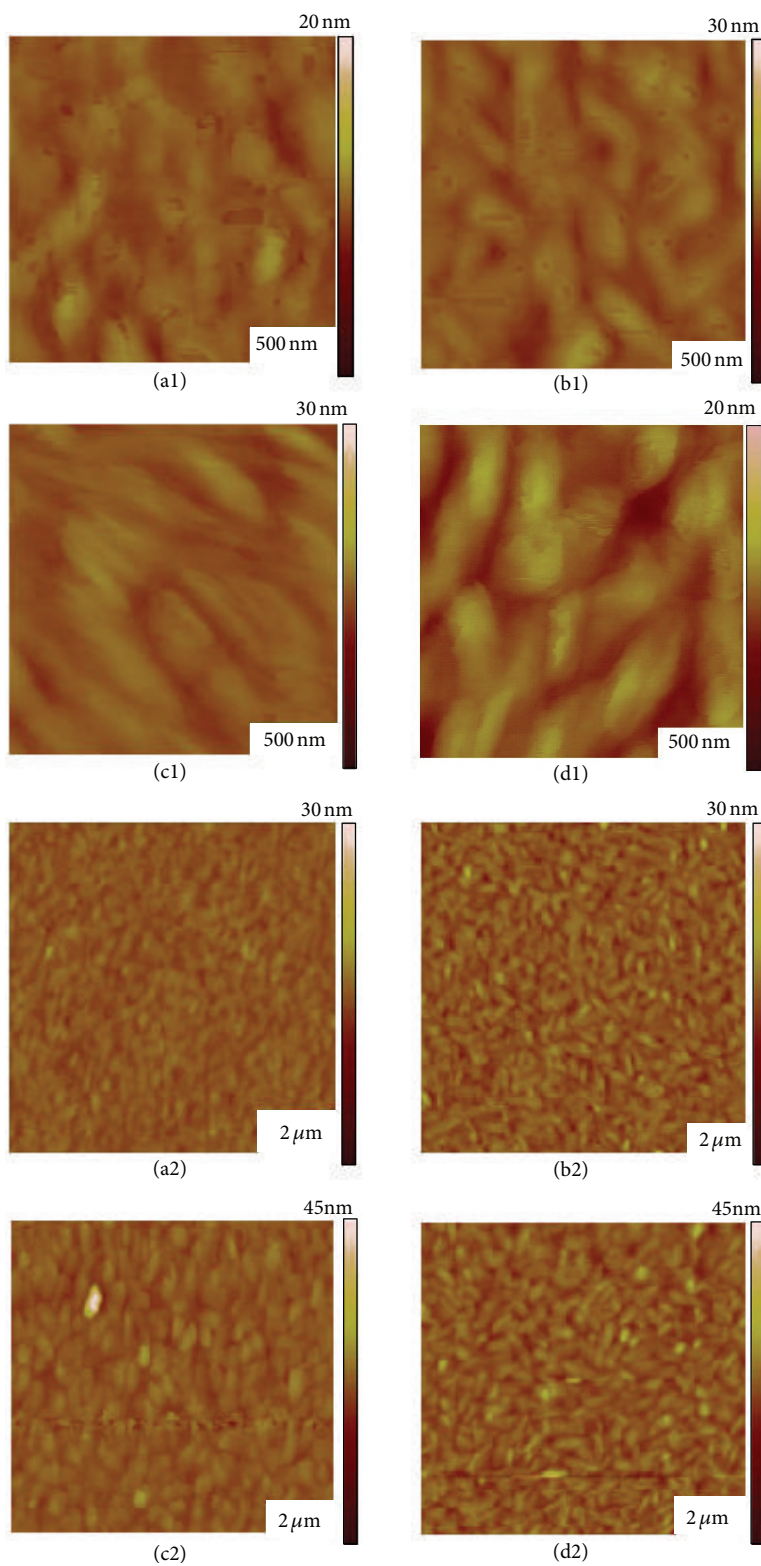


FIGURE 1: AFM images for PTCDI-C8 films with (a) 20, (b) 27, (c) 33, and (d) 45 nm thickness deposited on Si substrate at room temperature for scan sizes of  $500 \times 500 \text{ nm}^2$  and  $2 \times 2 \mu\text{m}^2$ .

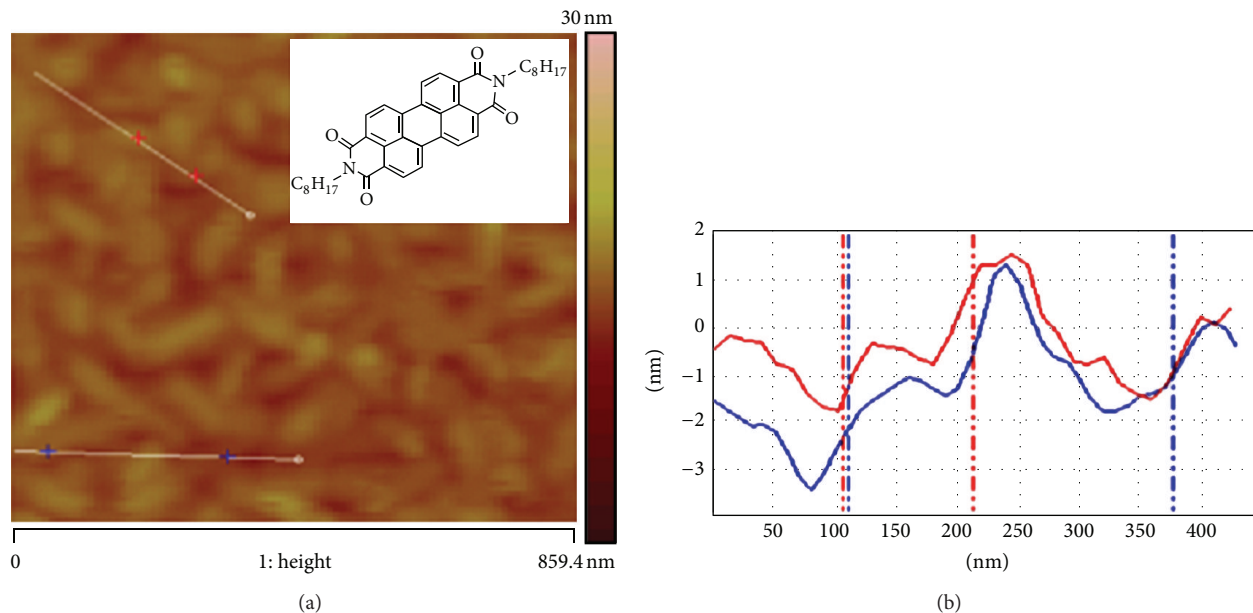


FIGURE 2: Line scans of the terraces which show monomolecular steps of 2 nm for 27 nm of PTCDI-C8 on Si. The inset presents the chemical structure of PTCDI-C8.

images were taken using a Veeco Multimode Scanning Probe Microscope AFM operated in tapping mode. X-ray reflectivity was performed using a Bruker-AXS D8-Discover high resolution X-ray diffractometer. This system utilizes a horizontal goniometer, fixed X-ray tube with a Cu anode (CuK  $\alpha$  radiation,  $\lambda = 0.15418$  nm), Göbel mirrors, Cu rotary absorber, 4-bounce Ge (022) monochromator, and Lynx Eye position sensitive detector (PSD) with automated Iris. The reflectivity data were analyzed using the Parratt formalism which takes into account multiple scattering effects [12]. Spectroscopic ellipsometry measurements were performed using a variable-incidence-angle ellipsometer from Woollam Company in the photon energy range of 1.4 to 3.5 eV and at the incident angles of 65, 70, and 75 degrees. All the experiments were carried out in the ambient condition. Summary of the material characterization is presented in the next section.

### 3. Results and Discussion

Figure 1 displays the typical topographical AFM images of 20, 27, 33, and 45 nm thick PTCDI-C8 films deposited on Si substrate at room temperature. PTCDI-C8 films display a relatively smooth surface morphology with needle-like features. These features which are randomly oriented in the film have a length of about several hundred nanometers. Planar terraces on the needles can be seen in the AFM images. The line scan of the terraces (Figure 2) reveals monomolecular steps of about 2 nm which is close to the film periodicity determined by the XRR data. The line scan has been performed over the area with the largest differences between the heights of the features. A summary of the roughness of the films with different thicknesses has been presented in Figure 3. As can be seen in this figure, the root mean square roughness

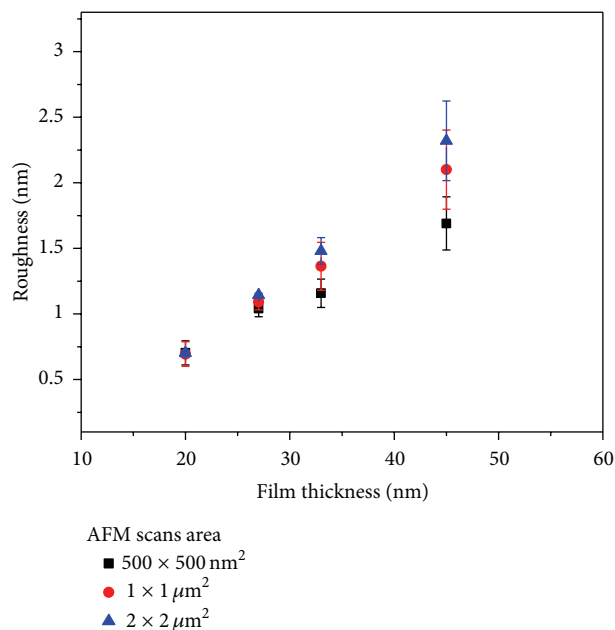


FIGURE 3: Plot of the surface roughness versus thickness of the PTCDI-C8 films deposited on Si substrates.

increases from 0.7 nm to 1.7 nm as the film thickness increases from 20 nm to 45 nm. Having a relatively smooth surface for thicker films suggests that the films display a wetting behavior on the Si substrates [13].

Furthermore, X-ray reflectivity was performed to evaluate the structural properties of PTCDI-C8 films. The results of the XRR studies are presented in Figure 4(a) and have been offset deliberately for better presentation. These reflectivity curves were analyzed using the Parratt formalism. In this

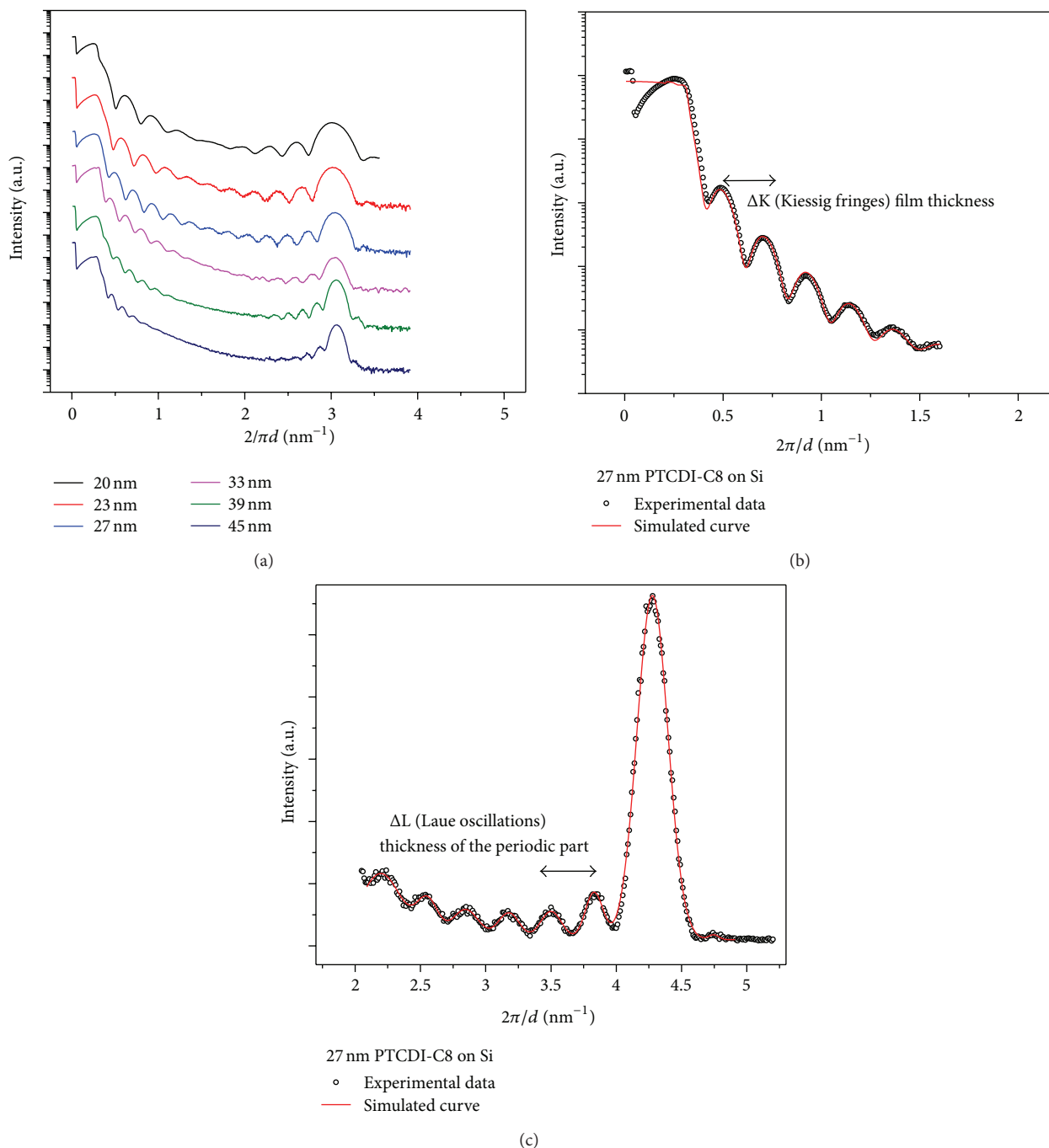


FIGURE 4: X-ray reflectivity curves for (a) different thicknesses of PTCDI-C8 films as well as the measured and simulated reflectivity data for (b) Kiessig fringes and (c) Laue oscillations for PTCDI-C8 film with 27 nm thickness.

model, the transmitted X-ray in the top-most layer serves as a new source for the scattering at the next lower interface [14]. Kiessig fringes at low angles as well as the Bragg peak with un-damped Laue oscillations indicate formation of films with a highly ordered structure. The low angle Kiessig fringes are related to the total film thickness and the Laue oscillations around the Bragg peak are related to the coherently ordered film thickness. Figures 4(b) and 4(c) show the measured and simulated reflectivity data for a 27 nm thick film of PTCDI-C8. Similarity of the widths of the Kiessig fringes with

the Laue oscillations around the Bragg peak suggests that PTCDI-C8 films are coherently ordered across their entire thickness.

The roughness and the thickness of the deposited films have been determined by a combination of techniques including AFM, ellipsometry, and XRR. A summary of the roughness analysis from AFM and XRR has been shown in Figure 5(a). Thickness data from ellipsometry and XRR is also summarized in Figure 5(b). As presented in these figures, the results of characterization from different techniques are

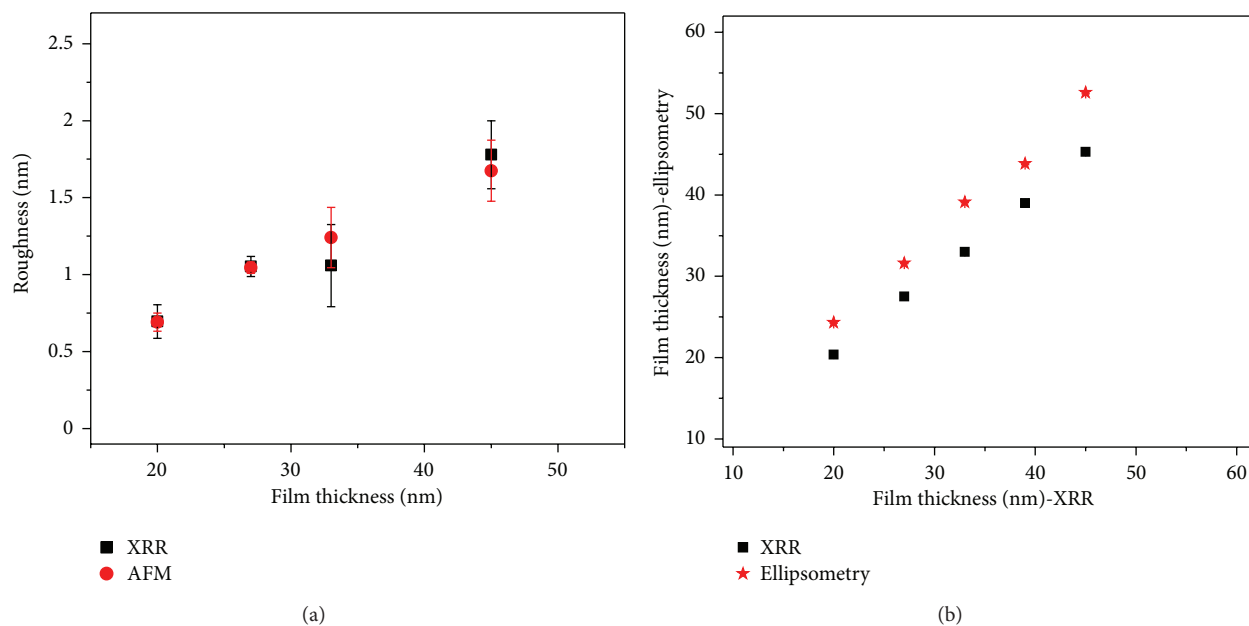


FIGURE 5: Comparing the measured and calculated (a) roughness from AFM and XRR data and (b) thickness from ellipsometry and XRR data. As can be seen in these figures, results from different methods match.

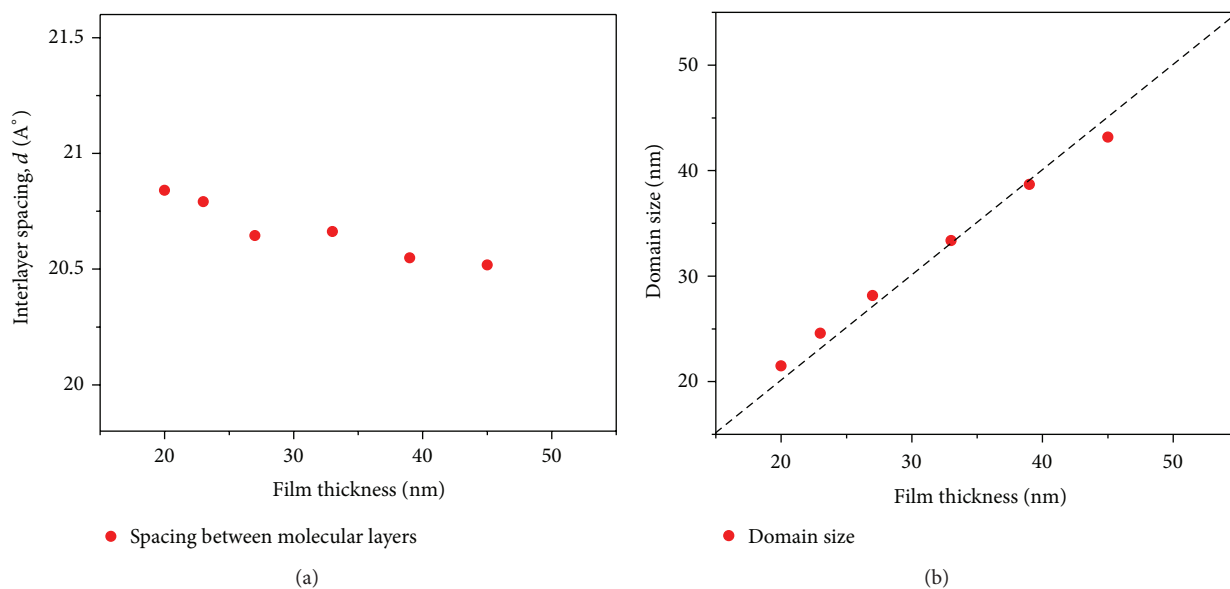


FIGURE 6: Calculated (a) interlayer spacing and (b) domain size for PTCDI-C8 films with different thicknesses.

similar. Among these techniques, XRR is the best method to characterize the structure of the materials in a thin film since it provides detailed information about the film roughness and thickness as well as molecular ordering and film morphology.

Moreover, the interlayer spacing ( $d$ ) can be determined from the diffraction peaks according to Bragg's equation,  $n\lambda = 2d \sin \theta$ , where  $n$  is the order of the diffraction peak and  $\theta$  is the scattering angle. A summary of the calculated values for PTCDI-C8 films with different thicknesses is presented in Figure 6(a). Calculated values for interlayer spacing are in good agreement with the height of the molecular terraces measured from AFM topographical images. In a simplified

way, considering negligible contribution from the strain, the mean size of the crystalline domains can be estimated from the inverse of the full width at half maximum (FWHM) of the Bragg peak using equation  $D \approx K\lambda/\beta \cos \theta$ , where  $K$  is the Scherrer constant,  $\lambda$  the wavelength,  $\beta$  the FWHM, and  $2\theta$  is the Bragg peak angular position. The domain sizes calculated for the different thicknesses of PTCDI-C8 films are presented in Figure 6(b). As can be seen in this plot, thicker films possess larger domain size and therefore sharper peaks compared to the thinner films. The size of the crystalline domains estimated from the X-ray reflectivity measurements is in the range of 20 to 40 nm for different thicknesses.

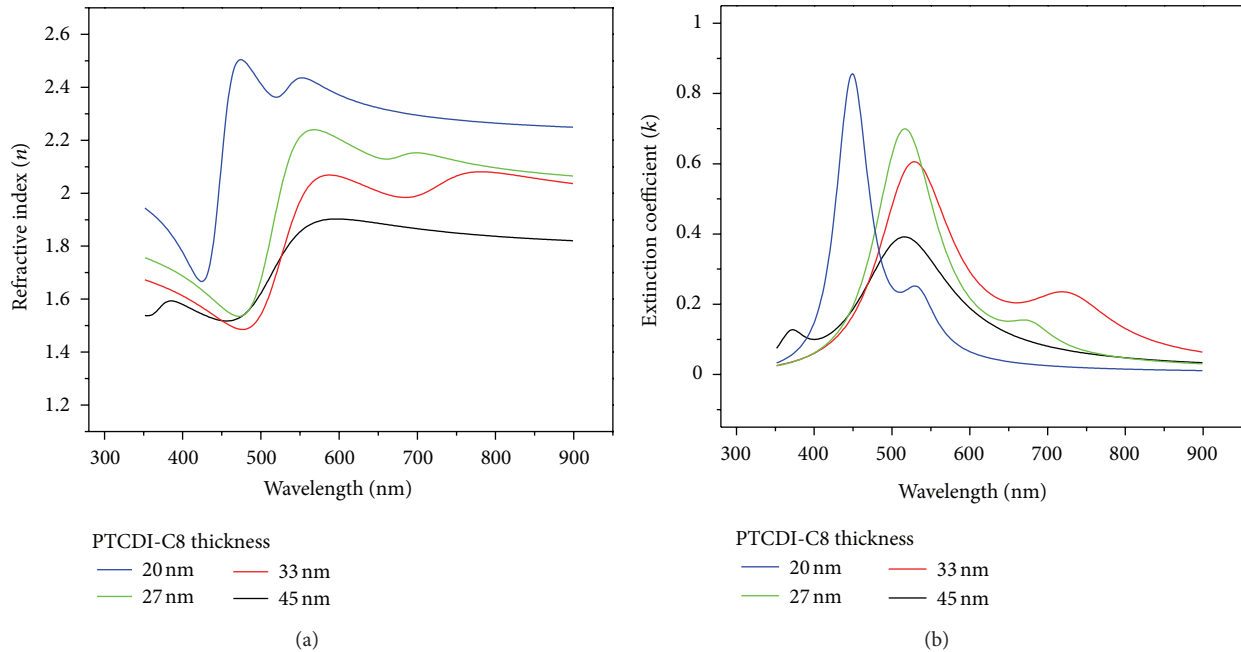


FIGURE 7: The (a) refractive indices ( $n$ ) and (b) extinction coefficients ( $k$ ) for PTCDI-C8 films with different thicknesses.

The fact that these values are considerably smaller than the grains size (needle-like features) observed in the AFM images indicates that the deposited films possess polycrystalline structure.

The refractive indices ( $n$ ) and extinction coefficients ( $k$ ) were extracted from the ellipsometry spectra of PTCDI-C8 thin films using Lorentz model. Figure 7 shows the ellipsometry results for different thicknesses of PTCDI-C8 films. Optical constants of some derivatives of perylenes family such as PTCDA and PTCDI-C13 have been reported previously in the literature [15]. However, the authors believe that their attempt to model optical spectra of PTCDI-C8 may be one of the only reported ones. As can be seen in these figures, for both  $n$  and  $k$  spectra, increasing the thickness of the film decrease the intensity of the peaks and shifts their position toward lower energies. The effects of thickness variation on the optical constants can be attributed to the change in the density of the defects in the films [16]. XRR studies revealed that thicker films possess larger crystalline domains, which modify the formation and the density of the defects inside the deposited films. Therefore, the differences in the optical properties of these films can be attributed to the thickness variation.

#### 4. Conclusions

In summary, in order to study the structural properties of PTCDI-C8 thin films, different thicknesses of this material have been deposited on  $\text{SiO}_2/\text{Si}$  substrates by vacuum thermal evaporator at room temperature. The effect of the thickness variation on the structural and optical properties of these films has been investigated performing AFM, XRR, and ellipsometry. The results of this study verify the existence of a very high internal molecular ordering within the PTCDI-C8 films

regardless of the thickness variation. The average sizes of the crystalline domains which have been extracted from the XRR analysis coincide with the film thickness. This implies the presence of a 3D crystalline structure across the entire thickness of the layered film. Therefore, the reported outstanding optical and electrical properties of organic semiconductor devices based on PTCDI-C8 can be attributed to the high degree of molecular packing observed for these films.

#### Acknowledgment

R. Rahimi has been partially supported through the WVNano Bridge Award at West Virginia University.

#### References

- [1] M. E. Gershenson, V. Podzorov, and A. F. Morpurgo, "Colloquium: electronic transport in single-crystal organic transistors," *Reviews of Modern Physics*, vol. 78, no. 3, pp. 973–989, 2006.
- [2] S. Tatemichi, M. Ichikawa, S. Kato, T. Koyama, and Y. Taniguchi, "Low-voltage, high-gain, and high-mobility organic complementary inverters based on  $\text{N,N}'$ -ditridecyl-3,4,9,10-perylene-tetracarboxylic diimide and pentacene," *Physica Status Solidi*, vol. 2, no. 2, pp. 47–49, 2008.
- [3] C. Rolin, K. Vasseur, S. Schols et al., "High mobility electron-conducting thin-film transistors by organic vapor phase deposition," *Applied Physics Letters*, vol. 93, no. 3, Article ID 033305, 2008.
- [4] R. Rahimi and D. Korakakis, "Organic thin film transistors based on pentacene and PTCDI as the active layer and  $\text{LiF}$  as the insulating layer," in *Proceedings of the Materials Research Society (MRS '09)*, vol. 1197, pp. 59–64, December 2009.
- [5] J. H. Oh, S. Liu, Z. Bao, R. Schmidt, and F. Würthner, "Air-stable n-channel organic thin-film transistors with high field-effect

- mobility based on N,N'-bis(heptafluorobutyl)-3,4,9,10-perylene diimide," *Applied Physics Letters*, vol. 91, no. 21, Article ID 212107, 3 pages, 2007.
- [6] R. T. Weitz, K. Amsharov, U. Zschieschang et al., "Organic n-channel transistors based on core-cyanated perylene carboxylic diimide derivatives," *Journal of the American Chemical Society*, vol. 130, no. 14, pp. 4637–4645, 2008.
- [7] M. Tolan, "X-ray scattering from soft-matter thin films," in *Springer Tracts in Modern Physics*, vol. 148, Springer, Heidelberg, Germany, 1999.
- [8] S. M. Mok, F. Yan, and H. L. W. Chan, "Organic phototransistor based on poly(3-hexylthiophene)/TiO<sub>2</sub> nanoparticle composite," *Applied Physics Letters*, vol. 93, no. 2, Article ID 023310, 2008.
- [9] R. J. Chesterfield, J. C. McKeen, C. R. Newman et al., "Organic thin film transistors based on N-alkyl perylene diimides: charge transport kinetics as a function of gate voltage and temperature," *Journal of Physical Chemistry B*, vol. 108, no. 50, pp. 19281–19292, 2004.
- [10] P. R. L. Malenfant, C. D. Dimitrakopoulos, J. D. Gelorme et al., "N-type organic thin-film transistor with high field-effect mobility based on a N,N'-dialkyl-3,4,9,10-perylene tetracarboxylic diimide derivative," *Applied Physics Letters*, vol. 80, no. 14, pp. 2517–2519, 2002.
- [11] T. N. Krauss, E. Barrena, X. N. Zhang et al., "Three-dimensional molecular packing of thin organic films of PTCDI-C 8 determined by surface X-ray diffraction," *Langmuir*, vol. 24, no. 22, pp. 12742–12744, 2008.
- [12] S. Karak, V. S. Reddy, S. K. Ray, and A. Dhar, "Organic photovoltaic devices based on pentacene/N,N'-dioctyl-3,4,9,10-perylenedicarboximide heterojunctions," *Organic Electronics*, vol. 10, no. 5, pp. 1006–1010, 2009.
- [13] J. O. Osso, F. Schreiber, V. Kruppa et al., "Controlled molecular alignment in phthalocyanine thin films on stepped sapphire surfaces," *Advanced Functional Materials*, vol. 12, no. 6-7, pp. 455–460, 2002.
- [14] L. G. Parratt, "Surface studies of solids by total reflection of x-rays," *Physical Review*, vol. 95, no. 2, pp. 359–369, 1954.
- [15] M. Stella, F. Villar, F. E. Rojas et al., "Optical and morphological characterization of PTCDI-C13," in *Proceedings of the Materials Research Society (MRS '08)*, vol. 1091, pp. 56–61, March 2008.
- [16] P. Prathap, N. Revathi, Y. P. Venkata Subbaiah, and K. T. Ramakrishna Reddy, "Thickness effect on the microstructure, morphology and optoelectronic properties of ZnS films," *Journal of Physics Condensed Matter*, vol. 20, no. 3, Article ID 035205, 2008.

## Research Article

# Silver Nanoparticle-Doped Titanium Oxide Thin Films for Intermediate Layers in Organic Tandem Solar Cell

Wanyi Nie, Robert C. Coffin, and David L. Carroll

Center for Nanotechnology and Molecular Materials, Department of Physics, Wake Forest University, Winston-Salem, NC 27109, USA

Correspondence should be addressed to David L. Carroll; [carroldl@wfu.edu](mailto:carroldl@wfu.edu)

Received 25 September 2012; Accepted 31 December 2012

Academic Editor: K. N. Narayanan Unni

Copyright © 2013 Wanyi Nie et al. This is an open access article distributed under the Creative Commons Attribution License, which permits unrestricted use, distribution, and reproduction in any medium, provided the original work is properly cited.

In this work we investigate the Ag nanoparticle doping of TiOx used as an intermediate layer between subcells of a tandem organic photovoltaic. We use a model polymer cell structure of P3HT:TiOx:PEDOT:P3HT to observe charge-trapping effects as a function of nanoparticle content in the TiOx, as determined by the shape of the dark and illuminated current voltage curves of the devices. There is a direct correlation between the amount of Ag nanoparticles in the TiOx, and interfacial charge buildup, and charge trapping being completely mitigated at around 0.2% mol. This suggests that such doping schemes might provide a simple approach to the creation and use of TiOx layers for tandem cells.

## 1. Introduction

Polymer-based organic solar cells in single-layer bulk heterojunction have now demonstrated power conversion efficiencies (PCEs) of between 7%–9% [1–3]. These efforts have improved the solar cell performance by modifying the chemical structure [4, 5] of the polymers or of the bulk heterojunction acceptor [6] which has yielded improvements to the filling factor (FF) through better packing and the short circuit current density ( $J_{sc}$ ) through smaller bandgaps. However, the PCE of such cells remains limited by the open circuit voltage ( $V_{oc}$ ) [7], which arises from the difference between donor highest occupied molecular orbital (HOMO) level and acceptor lowest unoccupied molecular orbital (LUMO) level [8, 9]. Given the optical absorption bandgap and the need to set the acceptor levels sufficiently below the polymer's LUMO for efficient exciton separation, increasing the  $V_{oc}$  in a single-layer bulk heterojunction device can be challenging.

A popular approach to increasing the  $V_{oc}$  in such circumstances is the use of a series-connected solar cell configuration: a “tandem solar cell,” in which two or three polymer solar cells with different optical bandgaps, matched across the solar spectrum, are stacked together [10]. Typically, in tandem devices, there is an interconnection layer (ICL) between the subcells that serve to allow current flow through

the device. This interlayer has to be sufficiently conductive and transparent for charge and light to pass unimpeded. This further requires the Fermi level to be in a specific range depending on the LUMO of the front-cell acceptor and HOMO of the back-cell donor for the charge collection and voltage add up. Finally, since this ICL can allow for the recombination of electrons generated by the front cell and the holes from the back cell (for noninverted subcells), mobility must be high, meaning no charge trapping. Examples of interlayers successfully demonstrated to meet some of these requirements and connect the subcells are ultrathin metal films of silver or gold [11, 12]; vacuum deposited metal oxide (i.e., indium tin oxide (ITO), molybdenum trioxide ( $MoO_3$ ) [13, 14] or solution processed metal oxides (such as Titanium Oxide and Zinc Oxide)) [15].

Most studies insert TiOx or ZnOx as an electron transport layer (ETL), together with poly(3,4-ethylenedioxythiophene) poly(styrenesulfonate) (PEDOT:PSS) between the front cell and back cell, that provides a region for holes generated by the front cell and electrons transported from the back cell. But these suffer from insufficient electron mobility and result in a space charge trapping that leads to a fill factor reduction in tandem devices using ZnO [16] and TiOx [17, 18] as ETL. However, when irradiated with UV light, such as from a solar simulator with the UV filter removed, mobility

is restored as a charge balance in both ZnO and TiOx cases [17–19]. This effect has been interpreted as UV-stimulated detrapping of charge traps between the conductive PEDOT, which can be treated as metallic hole conductor, and then type semiconductive metal oxide (TiOx or ZnOx) [16, 17]. We note that an opposite phenomenon has been observed in Pandey et al.'s work [20], and this could be attributed to the Fermi level variation owing to the surface states and impurities for nanoporous TiO<sub>2</sub> films mentioned in the literature, which is different from our method.

In this study, we present an alternative method for electron activation. Following the work of photosensors [21], we employ the use of silver nanoparticles to dope the metal oxide. Focusing on solution-processed TiOx, we show that improvements in the conductivity and charge carrier mobility can be similar to those in the UV-activated case [21, 22]. Similar effect has been observed by Liu and Nunzi [23] by depositing 1 nm gold nanoparticles between two subcells in an inverted tandem cell configuration for space charge removal, which confirms our observation. This is demonstrated in a model P3HT system; however, the results can be applied to polymer devices with different bandgaps in the subcells, allowing for more efficient spectral splitting and charge collection generally.

## 2. Experiment

The detailed recipe for the preparation of TiOx sol-gel solutions has been reported elsewhere in the literature [24, 25]. Briefly, the sol gel is prepared from the hydrolysis of titanium (IV) isopropoxide (Aldrich, 99.9%) by water with the present of nitric acid (HNO<sub>3</sub>) [26] as catalyst and acetylacetone as chelating agent [18] under vigorous stirring. The obtained clear gel is heated in an oven at 60°C for 24 hours and aged for three days. Silver doping was achieved by subsequently dissolving silver nitrate in distilled water and added in TiOx solution (0.2 w.t.% in ethanol) by 0.1 mol%, 0.2 mol%, 0.4 mol%, and 1.0 mol%. After white light illumination during stirring for 24 hours, silver nanoparticles will be formed in the solution.

Prepatterned indium tin oxide (ITO) coated glass substrates (Delta Technologies) were cleaned by detergent and ozone treated for 30 min after drying in a vacuum oven. A blend solution of regioregular poly(3-hexylthiophene) (P3HT) (Reike Metal) and phenyl-C61-butyric acid methyl ester (PCBM) (as received from NANO.C) at a ratio of 1:0.8 in chlorobenzene was spun cast onto the poly(3,4-ethylenedioxythiophene) poly(styrenesulfonate) (PEDOT:PSS 4083), a 40 nm hole transporting layer formed by spin coating at 4000 rpm for 45 seconds, coated substrates at 1500 rpm for 30 sec. A thin layer of TiOx with silver doping ratio of 0 mol% (D00), 0.1 mol% (D01), 0.2 mol% (D02), 0.4 mol% (D04), and 1.0 mol% (D10) was spin coated at 1000 rpm on top of active layer. After the second PEDOT:PSS (PH500) film (~100 nm) was formed and baked at 130°C for 10 min, the back cell from the same P3HT:PCBM blend solution was spun casted at 1500 rpm to keep the thickness the same as the front active film. After the film was dried, the devices were transferred

to a vacuum chamber ( $< 1.0 \times 10^{-6}$  torr) for LiF (0.3 nm) and aluminum (100 nm) back contact deposition.

The solar cells were tested using a standard AM 1.5 g solar simulator at 100 mW/cm<sup>2</sup>. The active area of the devices is carefully masked while testing and determined to be between 0.08~0.12 cm<sup>2</sup>. The current-voltage characteristics are collected by Keithley 230.

## 3. Result and Discussion

The formed TiOx particles in thin film by spun casting this solution on glass substrate can be seen in the Field Emission Scanning Electron Microscopy (FESEM) image in Figure 1. The particles are closely packed in the film with an average size of 30 nm, which is comparable to literature stated [27, 28]. The TEM images in Figure 1(b) confirm a uniform porous TiOx matrix formed by this sol-gel method. By adding silver nitrite water solution in the TiOx ethanol solution and illuminated with white light for 24 hours, the silver nanoparticles are decomposed from silver nitrite and distributed uniformly in the TiOx matrix with a size of 5~10 nm. This can be observed as black spots by TEM in Figure 1(c) comparing with the nondoped film.

With a work function of  $4.27 \text{ eV} \pm 0.05 \text{ eV}$ , the sol-gel-derived amorphous titanium oxide (TiOx) should act as an electron-transporting layer (ETL) [29] in the solar cell. To test the TiOx performance as ETL in single-junction device, solar cells in the structure of ITO/PEDOT:PSS(4083)/P3HT:PCBM/TiOx/Al were fabricated and characterized by the IV curve under one sun illumination as shown in Figure 2(a). It is clear that the device with nondoped TiOx film exhibits an “s-shaped” JV curve near Voc. This indicates that space charge has been built up between cathode and active layer due to the insufficient charge carrier mobility, which corresponds to a low filling factor of 0.405 [19]. Once a small amount of silver nanoparticles (0.1 mol%) are added, the trapped charge, as indicated by the JV curve shape, has been removed, and a higher fill factor can be achieved (FF = 0.446). This was confirmed by performing a JV measurement (Figure 2(b)) on a diode fabricated by inserting TiOx layer between ITO and aluminum. Further increasing the doping level raises the fill factor to 0.605 at 0.2 mol%.

Since the electron tends to go to a higher-energy level from acceptor LUMO (−3.7 eV) to cathode Fermi level (−4.06 eV), the electron transporting layer work function needs to be high enough to maintain the Voc. The nondoped TiOx layer work function was measured to be  $4.27 \pm 0.05 \text{ eV}$ , which is similar to other studies [17]. This suggests the silver nanoparticles (work function = 4.5~4.7 eV) increase the work function as expected. The Voc (~0.66 V ± 0.02) was relatively constant at low levels of doping between 0.1 mol% and 0.4 mol%. However, it starts to drop by 10% at a higher doping (1.0 mol%) due to the work function increase up to  $4.79 \text{ eV} \pm 0.03 \text{ eV}$  as measured.

The ICL in tandem cell serves as a charge recombination layer for electron transported from the acceptor of front cell and the hole generated by the back cell and has to be both transparent to visible radiation and electrically compatible

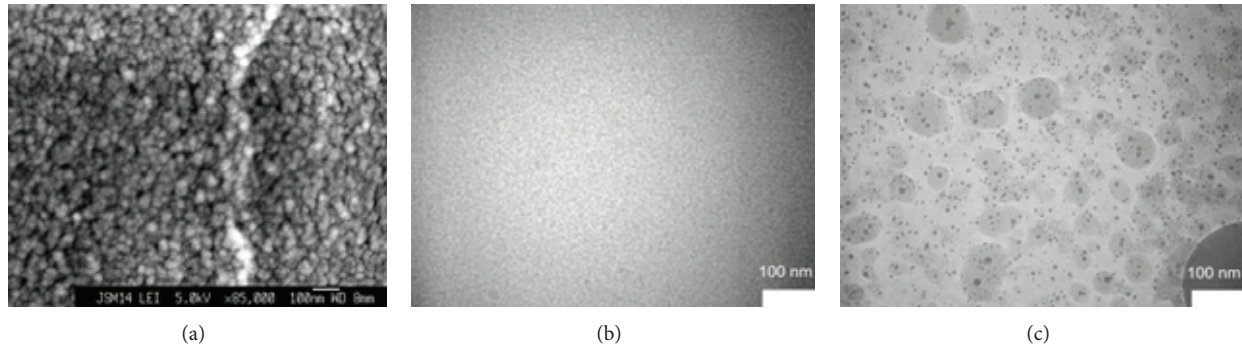


FIGURE 1: (a) FE-SEM image for TiOx thin film spun casted on glass substrate and TEM images on TiOx thin film (b) with 0.4 mol% silver nanoparticles and (c) without silver.

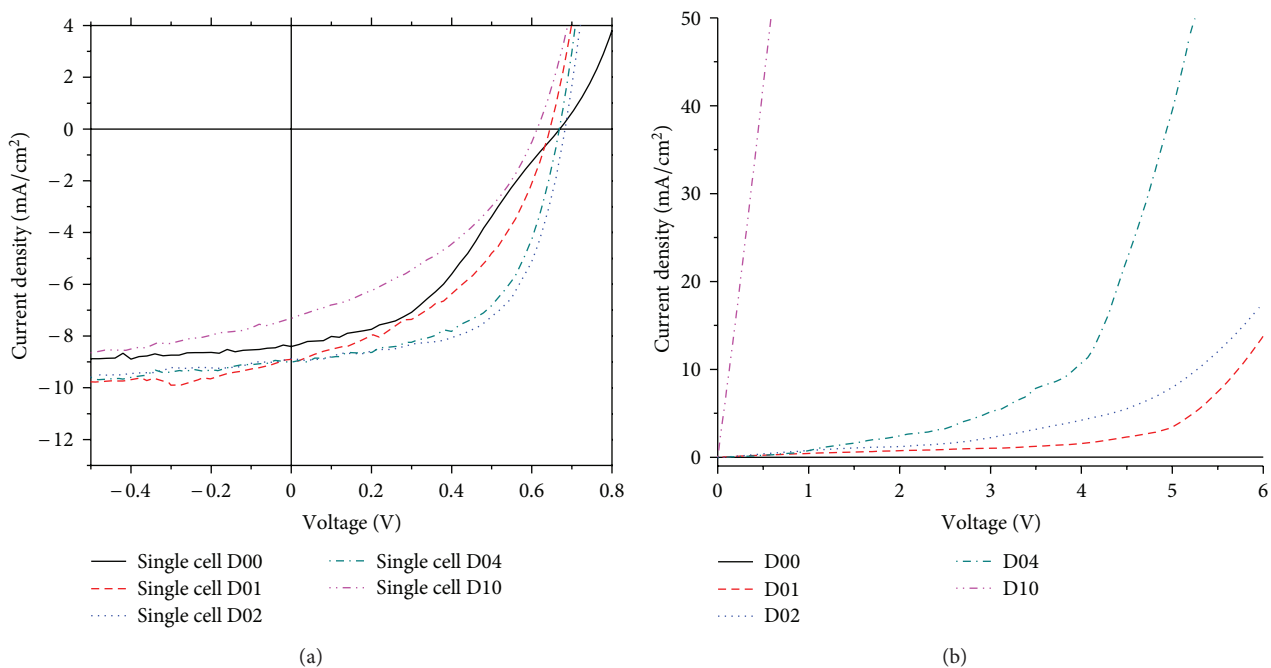


FIGURE 2: (a) Single junction device performance under standard illumination with TiOx as electron transport layer and (b) electron mobility in TiOx thin film diode without doping (black square) and doped by silver nanoparticles.

with the two subcells [30]. In our study, the combination of TiOx (with and without doping) as ETL and PEDOT:PSS as hole transport layer (HTL) was used as ICL between two identical absorbing layers composed of P3HT:PCBM at a ratio of 0.8. The thickness of the active layer of front cell has been kept the same as that in the back cell for all devices. The transparency of ETL thin films (with and without silver nanoparticles) was tested and is shown in Figure 3(a). It shows the transmission of 98% over the range of 300 nm to 1000 nm. The doped TiOx has a thickness of 20 nm in this study. In terms of the electrical behavior, however, the PEDOT has a work function of 5.2 eV, which induces a Schottky barrier at the interface between PEDOT and TiOx, leading to an insufficient charge recombination and voltage loss. The diodes in Figure 3(b) have a structure of ITO/PEDOT:PSS (PH500)/TiOx(silver)/Al, and the

undoped diode shows a Schottky curve while the doped diodes show ohmic contacts, which aids in charge transfer. From this we conclude that the doped layers should allow for light and charge transfer within the tandem structure.

The tandem devices were fabricated by inserting the above intermediate layers between two identical P3HT:PCBM bulk-heterojunction subcells, and the back contact was the combination of LiF and aluminum. As shown in Figure 4, the IV curve for the device fabricated by non-doped TiOx/PEDOT:PSS as interlayer has a “S” shaped curve under standard illumination near Voc, which is the Schottky barrier caused by the interface between TiOx and PEDOT:PSS, resulting in a low filling factor of 0.373 and Voc ~ 1.135 V with a potential loss. With a small amount of silver nanoparticles in TiOx (0.1 mol%), the “S” shape is partly corrected. Increasing the silver further to

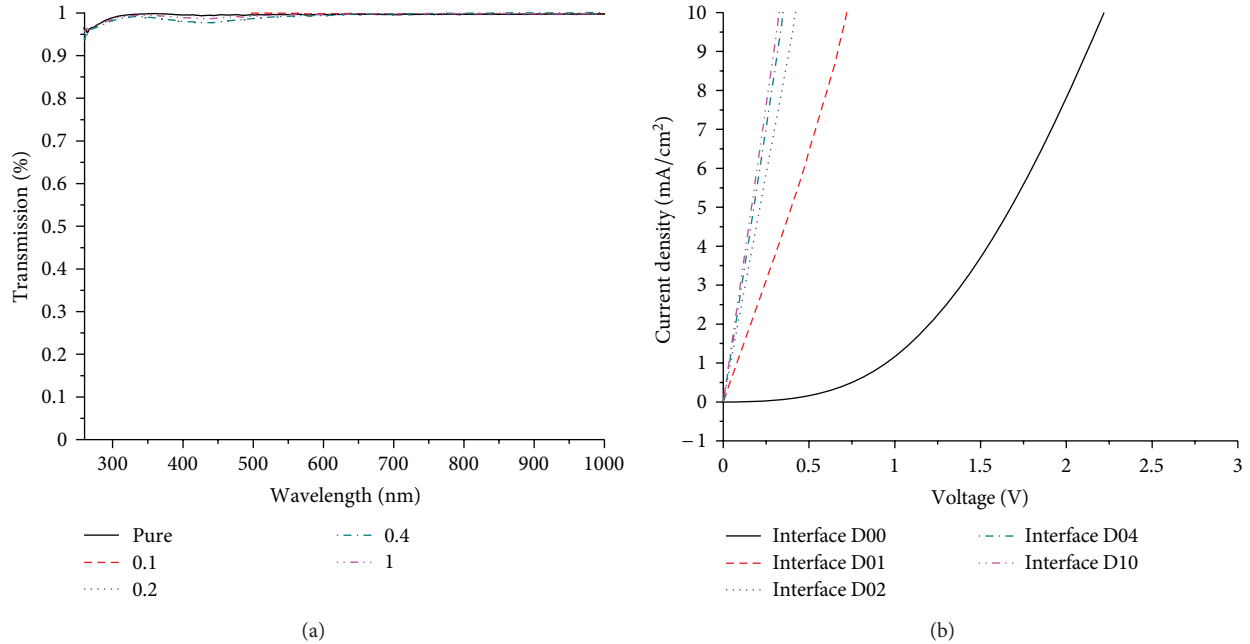


FIGURE 3: (a) IV characteristic of devices with structure of ITO/PEDOT:PSS/TiOx/Al diode and (b) transmission with TiOx thin film at changing amount of silver dopant from 0.1 mol% to 1 mol%.

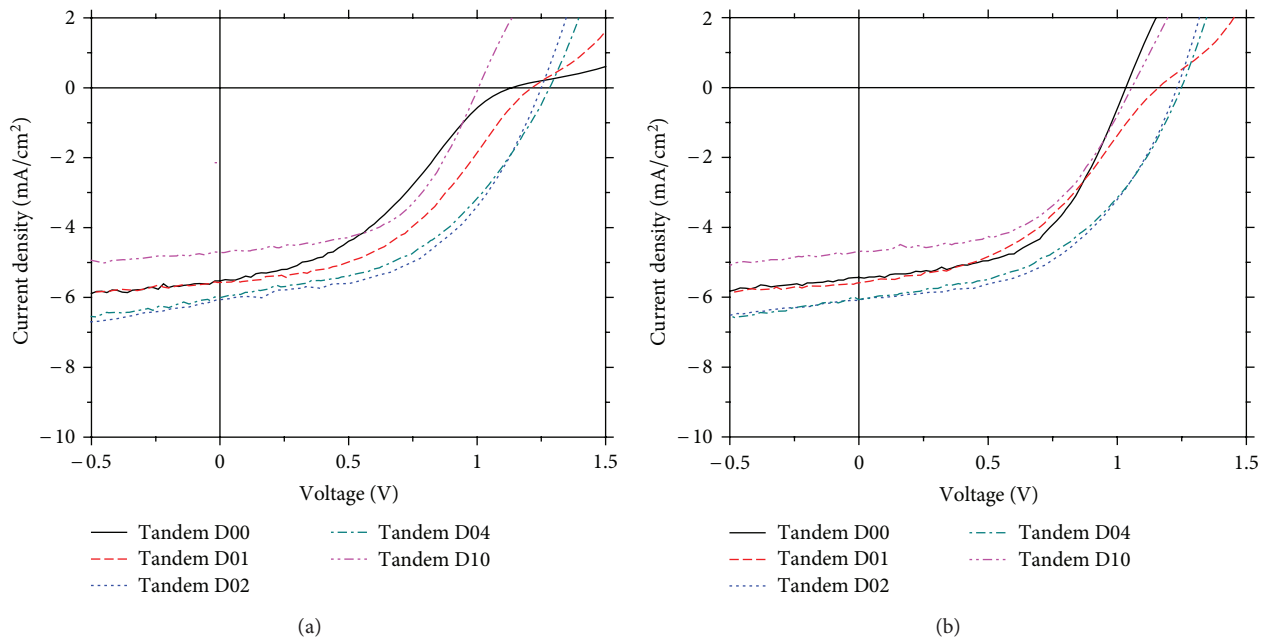


FIGURE 4: IV curves of single-junction device and tandem devices with doped and undoped TiOx interlayer under standard AM 1.5 solar simulator illumination when (a) UV filter not removed and (b) UV filter removed.

0.2~0.4 mol%, the Voc increased up to 1.25 V~1.28 V, which is roughly the sum over two single junction devices (0.66 V). The fill factor has also increased nearly 50% compared to nondoped device, resulting in a PCE  $\sim 3.63\% \pm 0.11$ . For a higher doping at 1.0 mol%, the device shows a slightly higher fill factor of 0.537 but a reduced Voc of 1.01 V which limits the PCE to around 2.5%.

By removing the UV filter in the solar simulator, and illuminating the undoped films, a similar effect was observed as in literature [18, 19]. The UV light activated the TiOx layer and removed the "S" curve near Voc, which increases FF from 0.314 up to 0.541. However, no significant change in the IV curve occurred by UV illumination for the doped TiOx layer devices.

## 4. Conclusion

This work investigated the use of Ag nanoparticles as a dopant for TiO<sub>x</sub> films used in organic photovoltaics. Single-junction devices were fabricated first, to test the TiO<sub>x</sub> performance as an electron transport layer. At the 0.2 mol% silver doping level of the TiO<sub>x</sub>, the single-layer devices exhibited improved rectification in the IV curve compared to the devices with nondoped film. In the model, tandem P3HT photovoltaic, where the TiO<sub>x</sub> is used as an interlayer for transfer, the nanoparticle dopant increased the charge mobility and removed the Schottky barrier between the second PEDOT:PSS layer. The tandem solar cells using doped TiO<sub>x</sub> film also exhibited the expected addition of the open-circuit voltage (1.28 V) for low doping levels. However, for higher Ag doping the open circuit voltage begins to drop indicating misalignment of the energy levels of the system. This work is applicable to tandem devices that utilize multiple bandgaps in the subcells and suggests that nanoparticle doping schemes may play an important role in band alignment and carrier mobility as well as light scattering.

## References

- [1] Y. Liang, Z. Xu, J. Xia et al., "For the bright future-bulk heterojunction polymer solar cells with power conversion efficiency of 7.4%," *Advanced Materials*, vol. 22, no. 20, pp. E135–E138, 2010.
- [2] Z. He, C. Zhong, X. Huang et al., "Simultaneous enhancement of open-circuit voltage, short-circuit current density, and fill factor in polymer solar cells," *Advanced Materials*, vol. 23, no. 40, pp. 4636–4643, 2011.
- [3] T. Y. Chu, J. Lu, S. Beaupré et al., "Bulk heterojunction solar cells using thieno[3,4-c]pyrrole-4,6-dione and dithieno[3,2-b:2',3'-d]silole copolymer with a power conversion efficiency of 7.3%," *Journal of the American Chemical Society*, vol. 133, no. 12, pp. 4250–4253, 2011.
- [4] H. J. Son, W. Wang, T. Xu et al., "Synthesis of fluorinated polythienothiophene-co-benzodithiophenes and effect of fluorination on the photovoltaic properties," *Journal of the American Chemical Society*, vol. 133, no. 6, pp. 1885–1894, 2011.
- [5] C. Piliago, T. W. Holcombe, J. D. Douglas, C. H. Woo, P. M. Beaujuge, and J. M. J. Fréchet, "Synthetic control of structural order in N-alkylthieno[3,4-c]pyrrole-4,6-dione-based polymers for efficient solar cells," *Journal of the American Chemical Society*, vol. 132, no. 22, pp. 7595–7597, 2010.
- [6] G. J. Zhao, Y. J. He, and Y. Li, "6.5% efficiency of polymer solar cells based on poly(3-hexylthiophene) and indene-C60 bisadduct by device optimization," *Advanced Materials*, vol. 22, no. 39, pp. 4355–4358, 2010.
- [7] P. Schlinsky, C. Waldauf, and C. J. Brabec, "Recombination and loss analysis in polythiophene based bulk heterojunction photodetectors," *Applied Physics Letters*, vol. 81, no. 20, p. 3885, 2002.
- [8] H. Hoppe and N. S. Sariciftci, "Organic solar cells: an overview," *Journal of Materials Research*, vol. 19, no. 7, pp. 1924–1945, 2004.
- [9] S. Gunes, H. Neugebauer, and N. Serdar Sariciftci, "Conjugated polymer-based organic solar cells," *Chemical Reviews*, vol. 107, pp. 1324–1338, 2007.
- [10] T. Ameri, G. Dennler, C. Lungenschmied, and C. J. Brabec, "Organic tandem solar cells: a review," *Energy and Environmental Science*, vol. 2, no. 4, pp. 347–363, 2009.
- [11] A. Yakimov and S. R. Forrest, "High photovoltage multiple-heterojunction organic solar cells incorporating interfacial metallic nanoclusters," *Applied Physics Letters*, vol. 80, no. 9, p. 1667, 2002.
- [12] M. Hiramoto, M. Suezaki, and M. Yokoyama, "Effect of thin gold interstitial-layer on the photovoltaic properties of tandem organic solar cell," *Chemistry Letters*, vol. 19, pp. 327–330, 1990.
- [13] D. W. Zhao, X. W. Sun, C. Y. Jiang, A. K. K. Kyaw, G. Q. Lo, and D. L. Kwong, "Efficient tandem organic solar cells with an Al/MoO<sub>3</sub> intermediate layer," *Applied Physics Letters*, vol. 93, Article ID 083305, 2009.
- [14] J. Sakai, K. Kawano, T. Yamanari et al., "Efficient organic photovoltaic tandem cells with novel transparent conductive oxide interlayer and poly(3-hexylthiophene): fullerene active layers," *Solar Energy Materials and Solar Cells*, vol. 94, no. 2, pp. 376–380, 2010.
- [15] J. Y. Kim, K. Lee, N. E. Coates et al., "Efficient tandem polymer solar cells fabricated by all-solution processing," *Science*, vol. 317, no. 5835, pp. 222–225, 2007.
- [16] J. Gilot, M. M. Wienk, and R. A. J. Janssen, "Double and triple junction polymer solar cells processed from solution," *Applied Physics Letters*, vol. 90, no. 14, Article ID 143512, 2007.
- [17] S. Sista, M. H. Park, Z. Hong et al., "Highly efficient tandem polymer photovoltaic cells," *Advanced Materials*, vol. 22, no. 3, pp. 380–383, 2010.
- [18] W. Chung, H. Lee, W. Lee et al., "Solution processed polymer tandem cell utilizing organic layer coated nano-crystalline TiO<sub>2</sub> as interlayer," *Organic Electronics*, vol. 11, pp. 521–528, 2010.
- [19] F. Verbakel, S. C. J. Meskers, and R. A. J. Janssen, "Electronic memory effects in diodes from a zinc oxide nanoparticle-polystyrene hybrid material," *Applied Physics Letters*, vol. 89, no. 10, Article ID 102103, 2006.
- [20] A. K. Pandey, J. M. Nunzi, H. Wang et al., "Reverse biased annealing: effective post treatment tool for polymer/nanocomposite solar cells," *Organic Electronics*, vol. 8, no. 4, pp. 396–400, 2007.
- [21] A. Zaleska, "Doped-TiO<sub>2</sub>: a review," *Recent Patents on Engineering*, vol. 2, no. 3, pp. 157–164, 2008.
- [22] M. K. Seery, R. George, P. Floris, and S. C. Pillai, "Silver doped titanium dioxide nanomaterials for enhanced visible light photocatalysis," *Journal of Photochemistry and Photobiology A*, vol. 189, no. 2–3, pp. 258–263, 2007.
- [23] F. Liu and J. M. Nunzi, "Air stable hybrid inverted tandem solar cell design," *Applied Physics Letters*, vol. 99, no. 6, Article ID 063301, 2011.
- [24] P. V. Kamat, I. Bedja, and S. Hotchandani, "Photoinduced charge transfer between carbon and semiconductor clusters. One-electron reduction of C60 in colloidal TiO<sub>2</sub> semiconductor suspensions," *The Journal of Physical Chemistry*, vol. 98, pp. 9137–9142, 1994.
- [25] A. Zaban, S. Ferrere, J. Sprague, and B. A. Gregg, "pH-dependent redox potential induced in a sensitizing dye by adsorption onto TiO<sub>2</sub>," *Journal of Physical Chemistry B*, vol. 101, no. 1, pp. 55–57, 1997.
- [26] B. E. Yoldas, "Hydrolysis of titanium alkoxide and effects of hydrolytic polycondensation parameters," *Journal of Materials Science*, vol. 21, no. 3, pp. 1087–1092, 1986.
- [27] Z. Zhang, C. C. Wang, R. Zakaria, and J. Y. Ying, "Role of particle size in nanocrystalline TiO<sub>2</sub>-based photocatalysts," *Journal of Physical Chemistry B*, vol. 102, no. 52, pp. 10871–10878, 1998.

- [28] H. Sakai, H. Kawahara, M. Shimazaki, and M. Abe, "Preparation of ultrafine titanium dioxide particles using hydrolysis and condensation reactions in the inner aqueous phase of reversed micelles: effect of alcohol addition," *Langmuir*, vol. 14, no. 8, pp. 2208–2211, 1998.
- [29] J. Y. Kim, S. H. Kim, H. H. Lee et al., "New architecture for high-efficiency polymer photovoltaic cells using solution-based titanium oxide as an optical spacer," *Advanced Materials*, vol. 18, no. 5, pp. 572–576, 2006.
- [30] Y. Yuan, J. Huang, and G. Li, "Intermediate layers in tandem organic solar cells," *Green*, vol. 1, pp. 65–80, 2011.

## Research Article

# MEH-PPV and PCBM Solution Concentration Dependence of Inverted-Type Organic Solar Cells Based on Eosin-Y-Coated ZnO Nanorod Arrays

Riski Titian Ginting,<sup>1</sup> Chi Chin Yap,<sup>1</sup> Muhammad Yahaya,<sup>1</sup> and Muhamad Mat Salleh<sup>2</sup>

<sup>1</sup> School of Applied Physics, Faculty of Science and Technology, Universiti Kebangsaan Malaysia, 43600 Bangi, Selangor, Malaysia

<sup>2</sup> Institute of Microengineering and Nanoelectronics (IMEN), Universiti Kebangsaan Malaysia, 43600 Bangi, Selangor, Malaysia

Correspondence should be addressed to Chi Chin Yap; ccyap@ukm.my

Received 1 August 2012; Revised 29 November 2012; Accepted 29 November 2012

Academic Editor: Manoj A. G. Nambuthiry

Copyright © 2013 Riski Titian Ginting et al. This is an open access article distributed under the Creative Commons Attribution License, which permits unrestricted use, distribution, and reproduction in any medium, provided the original work is properly cited.

The influence of polymer solution concentration on the performance of chlorobenzene- (CB-) and chloroform- (CF-) based inverted-type organic solar cells has been investigated. The organic photoactive layers consisted of poly(2-methoxy-5-(2-ethyl hexyloxy)-1,4-phenylenevinylene) (MEH-PPV) and (6,6)-phenyl C<sub>61</sub> butyric acid methyl ester (PCBM) were spin coated from CF with concentrations of 4, 6, and 8 mg/mL and from CB with concentrations of 6, 8, and 10 mg/mL onto Eosin-Y-coated ZnO nanorod arrays (NRAs). Fluorine doped tin oxide (FTO) and silver (Ag) were used as electron collecting electrode and hole collecting electrode, respectively. Experimental results showed that the short circuit current density and power conversion efficiency increased with decrease of solution concentration for both CB and CF devices, which could be attributed to reducing charge recombination in thinner photoactive layer and larger contact area between the rougher photoactive layer and Ag contact. However, the open circuit voltage decreased with decreasing solution concentration due to increase of leakage current from ZnO NRAs to Ag as the ZnO NRAs were not fully covered by the polymer blend. The highest power conversion efficiencies of  $0.54 \pm 0.10\%$  and  $0.87 \pm 0.15\%$  were achieved at the respective lowest solution concentrations of CB and CF.

## 1. Introduction

Rapid development in enhancing the performance of organic solar cells (OSCs) for the past few years by utilizing bulk heterojunction (BHJ) devices has enabled power conversion efficiency (PCE) up to 10.6% to be achieved [1]. In the case of BHJ conventional device structure, an active layer which consists of polymer donor and acceptor material is normally sandwiched between indium tin oxide (ITO) anode and aluminium (Al) cathode [2]. Poly(3,4-ethylenedioxythiophene):poly(styrenesulfonate) or PEDOT:PSS which plays role as conductive hole transport layer (HTL) is commonly introduced in between organic photoactive layer and ITO anode [3]. However, due to strong acidic nature of PEDOT:PSS, instability between the interface of ITO/PEDOT:PSS could create defect site and thus leading to deteriorated device

performance [4, 5]. Moreover, oxidation of low work function Al electrode (4.28 eV) in air could also lead to instability at the interface between metal and organic photoactive layer [6]. In order to solve these issues, inverted configuration with low work function metal or metal oxides materials as electron transporting layer and high work function metal (e.g., silver, gold) as hole collection electrode have been introduced to improve the stability of the device [6, 7]. Lately, a lot of attention towards inverted OSCs with various metal oxide nanostructures as electron transporting layer have been developed, such as ZnO [8–14], TiO<sub>2</sub> [15–19], alkali-metal oxide cesium carbonate (Cs<sub>2</sub>CO<sub>3</sub>) [20, 21], and others [22, 23]. The environmental-friendly and low-cost ZnO nanorods arrays (NRAs) can be grown at low temperature (below 100°C) by hydrothermal method [24]. The ZnO NRAs not only have good electron collecting and transporting property

in the inverted OSCs hybridized with the polymer blend, but also can provide larger interface surface area to improve photocurrent and efficiency [25].

Recently, much effort has been focused on utilizing blend film of poly(3-hexylthiophene) (P3HT) and (6,6)-phenyl C<sub>61</sub> butyric acid methyl ester (PCBM) as photoactive layer in ZnO NRAs-based inverted OSCs [19–23]. Various P3HT-PCBM processing parameters such as solvent selection, solution concentration, and spin coating speed have been investigated to optimize the solar cell performance [25, 26]. Takanezawa et al. [25] reported that thicker organic photoactive layer deposited by using higher solution concentration or lower spin coating speed results in better power conversion efficiency as a consequence of improved optical absorption and short circuit current density. Meanwhile, Chou et al. [26] demonstrated that organic photoactive layer drying time could be lengthened by lowering the spin coating speed, hence leading to improved photovoltaic performance as a result of better polymer crystallinity, increased thickness, and enhanced infiltration of photoactive layer. However, little attention has been given to poly[2-methoxy-5-(2'-ethylhexyloxy)-p-phenylenevinylene] (MEH-PPV) blended with PCBM as photoactive layer in the similar OSCs. MEH-PPV has broad optical absorption region 400–600 nm and also higher hole mobility compared to electron mobility [27].

The present work reports on the effects of MEH-PPV and PCBM solution concentration on the performance of inverted-type OSCs based on Eosin-Y-coated ZnO NRAs. Eosin-Y organic dye, a low-cost alternative to expensive Ru-complexes dye, has good absorption property and is able to increase the wettability of ZnO surface [28]. Different solution concentrations of MEH-PPV and PCBM were prepared from chlorobenzene (CB) and chloroform (CF). The short circuit current density and power conversion efficiency increased, whereas the open circuit voltage decreased with the reduction of solution concentration. The optimum power conversion efficiencies of  $0.54 \pm 0.10\%$  and  $0.87 \pm 0.15\%$  were achieved at the respective lowest solution concentration of CB and CF devices.

## 2. Experimental Methods

**2.1. Device Fabrication.** Inverted OSCs with fluorine doped tin oxide (FTO)/Eosin-Y-coated ZnO NRAs/MEH-PPV and PCBM(1:2)/Ag structure were constructed. The FTO ( $\sim 15 \Omega/\text{sq}$ ) substrates were ultrasonically cleaned by using acetone and 2-propanol each for 15 min. The ZnO seed layer was spin coated on top of precleaned substrates for 3 times from an equimolar solution (0.2 M) of zinc acetate dehydrate ( $\text{Zn}(\text{O}_2\text{CCH}_3)_2 \cdot (\text{H}_2\text{O})_2$ ) and diethanolamine (DEA) in ethanol followed by annealing at 300°C for one hour in air. The hydrothermal growth of ZnO NRA was done by immersing ZnO seed coated substrates into an equimolar aqueous solution (40 mM) of zinc nitrate hexahydrate ( $\text{Zn}(\text{NO}_3)_2 \cdot 6\text{H}_2\text{O}$ ) and hexamethylenetetramine (HMT) at 90°C for 45 min in a laboratory oven. The dye coating was performed by spin coating a thin layer of Eosin-Y from a 0.3 mM acetone solution onto ZnO NRAs. The MEH-PPV

with molecular weight 40,000–70,000 g mol<sup>-1</sup> and PCBM were purchased from Sigma-Aldrich and Nano-C, respectively. MEH-PPV and PCBM (1:2 by weight) were dissolved in two different solvents, namely chloroform (CF) and chlorobenzene (CB) at various concentrations. CF solutions with concentration of 4 mg/mL to 8 mg/mL and CB solutions with concentration of 6 mg/mL to 10 mg/mL were spin-coated on top of Eosin-Y-coated ZnO NRAs. The spinning speed and spinning time were fixed at 1000 rpm and 60 s, respectively. Finally, the silver (Ag) contact (200 nm) was deposited by using magnetron sputtering under vacuum ( $\sim 10^{-3}$  Torr) by flowing Argon (Ar) gas at 45 cc/min. During sputtering process, a slow deposition rate  $\sim 0.17 \text{ nm s}^{-1}$  was used in order to avoid the damage of organic photoactive layer. Furthermore, in order to oxidize silver, pure oxygen gas was introduced during sputtering process into the vacuum chamber at a flow rate of 5 cc/min. It was believed that oxidation of Ag will increase its work function from 4.3 to 5.0 eV, which in turn facilitate hole collection from donor materials to Ag and improve the cells performance [29]. Four devices for each solution concentration were fabricated.

**2.2. Device Characterization.** The absorption spectra of blend films consisted of organic photoactive layer and Eosin-Y-coated ZnO NRAs were investigated using a Perkin Elmer Lambda 900 UV-Vis spectrophotometer. The cross-sectional images of organic photoactive layer deposited on Eosin-Y-coated ZnO NRAs were recorded by using Carl Zeiss Supra 55VP Field Emission Scanning Electron Microscope (FESEM). The surface morphology of the organic photoactive layers was investigated by using Ntegra Prima NT-MDT scanning probe microscope under ambient condition at %RH  $\sim 68\%$  and room temperature 26°C. The *J-V* characteristics of the devices were measured with Keithley 237 SMU under illumination at 100 mW/cm<sup>2</sup> from a solar simulator with AM 1.5 G filter. The active area of the devices was defined as 0.07 cm<sup>2</sup> by using mask. The incident photon to current conversion efficiency (IPCE) values was measured using Newport IPCE system at a chopping frequency of 10 Hz. The above device fabrication and measurements were conducted under ambient atmosphere (without encapsulation).

## 3. Results and Discussion

Figure 1 shows the optical absorption properties of blend films of organic photoactive layer and Eosin-Y-coated ZnO NRAs. Broad absorption from 400 nm up to 600 nm is correlated with MEH-PPV [30], whereas absorption below 400 nm is contributed by PCBM and ZnO NRAs [31]. The absorption increased with solution concentration for both CF and CB. It has been reported that enhanced absorption in the long wavelength range of the polymer indicates the increase in crystallinity and hole mobility of the polymer [32]. However, the shape of absorption spectra of MEH-PPV and PCBM blend film (in the range of 400–600 nm) showed no notable changes with different solvents and solution concentration, suggesting no significant different in crystallinity and hole mobility of the polymer. The Eosin-Y-coated ZnO

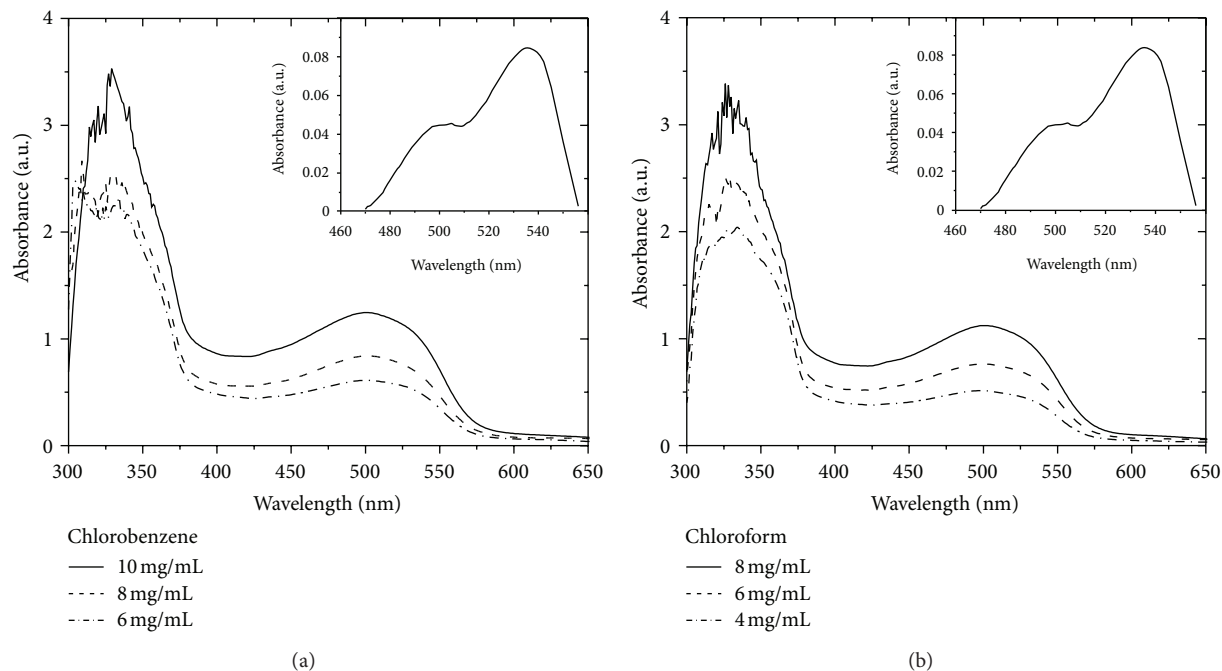


FIGURE 1: The absorption spectra of blend films of Eosin-Y-coated ZnO NRAs and organic photoactive layer deposited from (a) CB and (b) CF solvents at various concentrations. Inset shows the absorption spectra of Eosin-Y-coated ZnO NRAs in the region 440–560 nm.

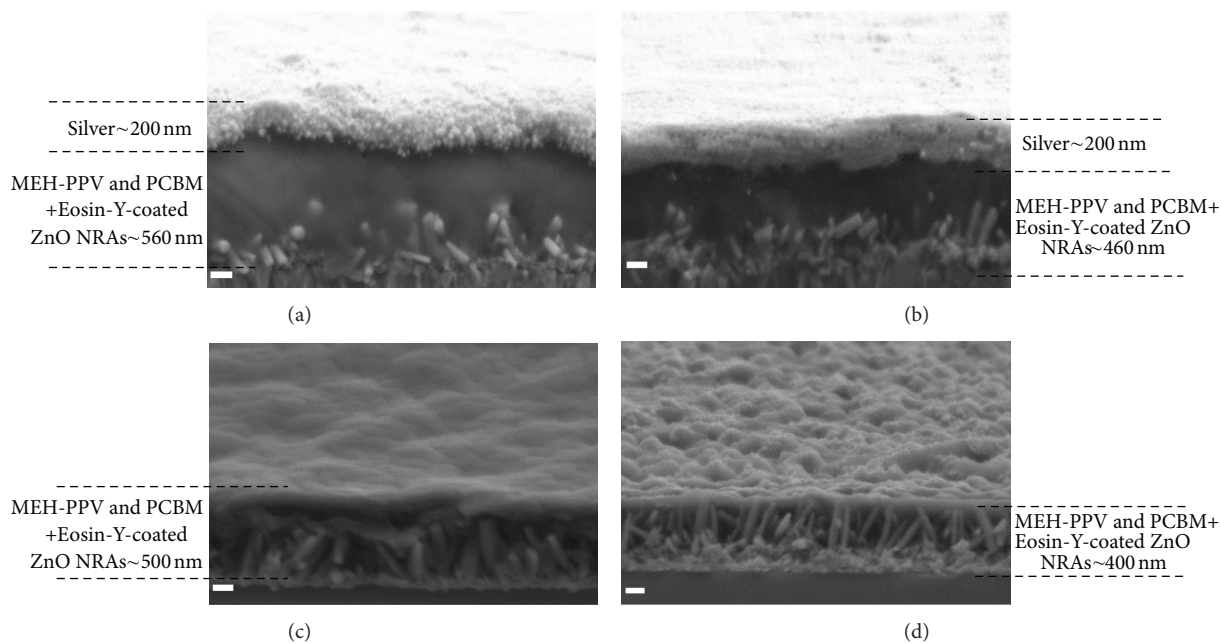


FIGURE 2: Cross-sectional FESEM images of devices prepared from CB at concentrations (a) 10 mg/mL (b) 6 mg/mL and prepared from CF at concentrations (c) 8 mg/mL, (d) 4 mg/mL (scale bar: 100 nm).

NRAs exhibited absorption in visible region from 440 nm to 560 nm (inset of Figure 1) and two absorption peaks at 500 nm and 530 nm corresponding to the monomeric and dimeric forms of Eosin-Y were observed [33]. The intensity of Eosin-Y absorption was much lower than that of MEH-PPV, suggesting Eosin-Y had a little contribution to the overall

absorption of device. However, the existence of thin layer dye on top of ZnO NRAs may enhance the charge transfer efficiency at the MEH-PPV/ZnO NRAs interface and also improve the wetting state of ZnO NRAs [34].

Figure 2 shows typical cross-sectional images of devices prepared from CB and CF at different concentrations. ZnO

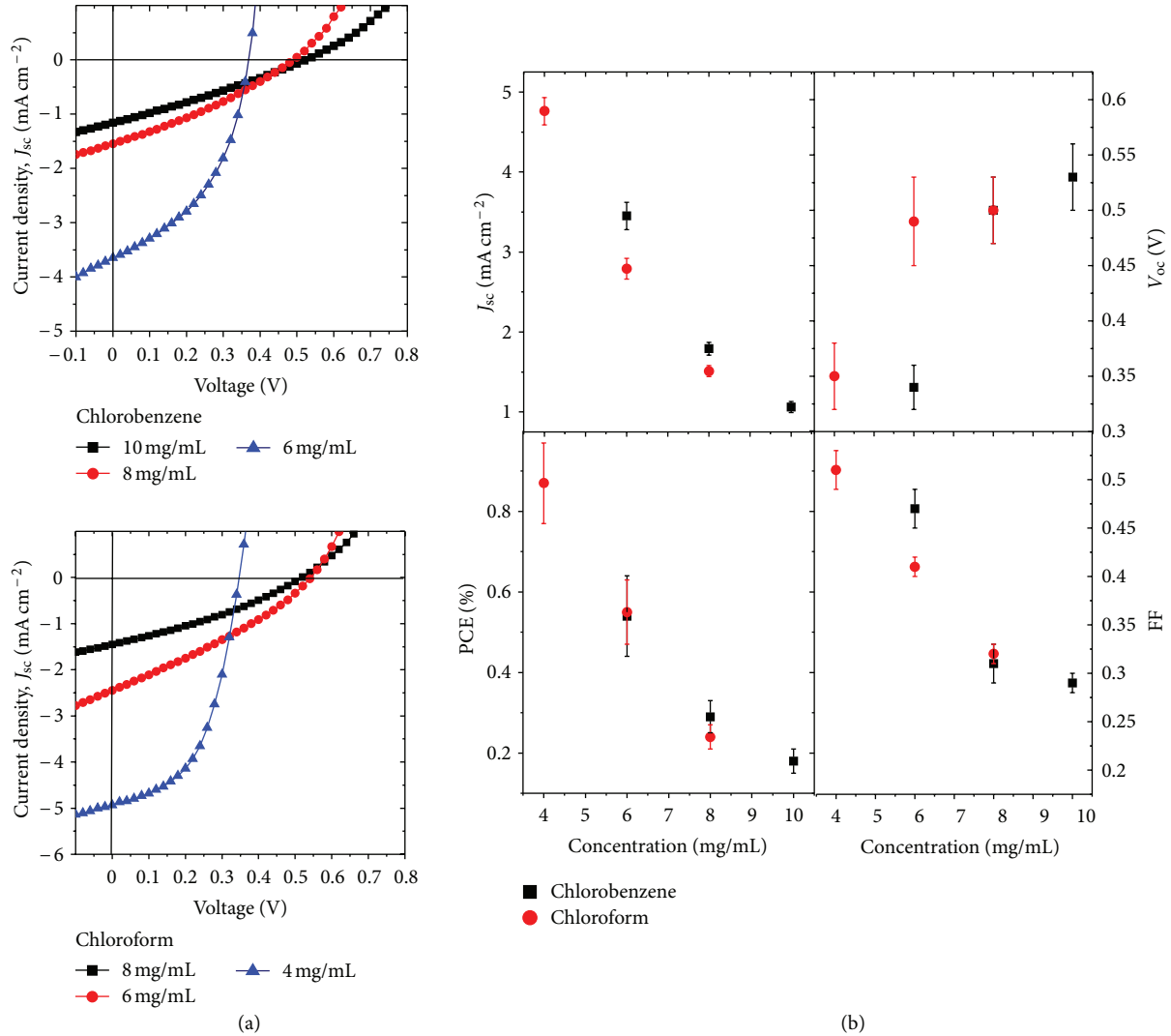


FIGURE 3: (a)  $J$ - $V$  characteristics of devices prepared from different CB and CF solution concentrations, (b) photovoltaic parameters of devices as a function of solution concentration.

nanorods with diameter ranging from 50 nm to 80 nm and with length up to 300 nm were obtained. The total thickness of the blend films prepared from CB and CF reduced from  $\sim 560$  nm to  $\sim 460$  nm and from  $\sim 500$  nm and  $\sim 400$  nm, respectively, with decrease of solution concentration. This is consistent with absorption result shown above where the absorption increased with increasing solution concentration, indicating formation of thicker blend film. In addition, it can be clearly seen that the infiltration of organic blend prepared from CB into the spacing between Eosin-Y-coated ZnO nanorods was better than that prepared from CF, as indicated by the increased number of voids appeared in the interspaces between ZnO nanorods. The polymer prepared from a higher boiling point solvent has longer time to effectively infiltrate into the spacing between ZnO nanorods and gives enough time for polymer chain to self-organized [35]. Therefore, the poor infiltration could be attributed to lower boiling point of CF ( $\sim 61^\circ\text{C}$ ) as compared to CB ( $\sim 131^\circ\text{C}$ ).

The  $J$ - $V$  characteristics of typical devices under illumination of a simulated AM 1.5 sunlight at  $100 \text{ mW/cm}^2$  are shown in Figure 3(a), whereas the statistical data for photovoltaic parameters obtained from a series of four individual devices for each parameter are plotted in Figure 3(b). The short-circuit current density ( $J_{sc}$ ), fill factor (FF) and power conversion efficiency (PCE) increased with decreasing solution concentration for both CB- and CF-based devices, whereas the open circuit voltage ( $V_{oc}$ ) exhibited opposite behavior. Both CB- and CF-based devices showed the highest PCE at respective lowest solution concentration. The device prepared from CB at concentration of 6 mg/mL exhibited the highest PCE of  $0.54 \pm 0.10\%$  with  $J_{sc}$  of  $3.45 \pm 0.17 \text{ mA cm}^{-2}$ ,  $V_{oc}$  of  $0.34 \pm 0.02 \text{ V}$  and FF of  $0.48 \pm 0.02$ . In the case of CF, the highest PCE of  $0.87 \pm 0.15\%$  was achieved at the concentration of 4 mg/mL, with  $J_{sc}$  of  $4.76 \pm 0.17 \text{ mA cm}^{-2}$ ,  $V_{oc}$  of  $0.35 \pm 0.03 \text{ V}$ , and FF of  $0.51 \pm 0.02$ . However, further reduction of polymer solution concentration results in very

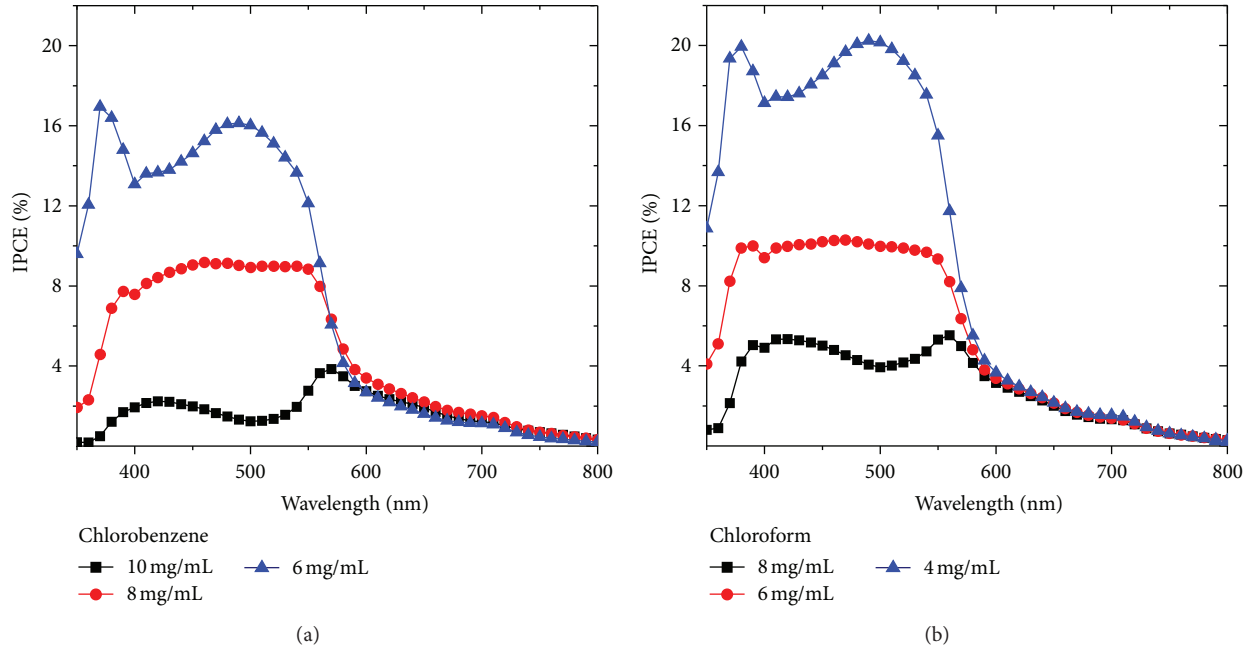


FIGURE 4: The IPCE spectra of devices prepared from different CB and CF solution concentrations.

low  $V_{oc} < 0.2$  V and low  $J_{sc} < 0.75$  mA cm<sup>-2</sup> for both CB and CF devices (not shown here). The series resistance ( $R_s$ ) and shunt resistance ( $R_{sh}$ ) were determined from the slopes at  $V_{oc}$  and  $J_{sc}$  in the  $J$ - $V$  curve, respectively. The enhancement of  $J_{sc}$  with decreasing solution concentration could be correlated with the organic photoactive layer thickness. It is generally accepted that increase in thickness results in more excitons due to higher absorption. However, the charge recombination rate also increases with thickness, resulting in lower  $J_{sc}$ . In contrast to study obtained on P3HT and PCBM-based inverted-type organic solar cell [25], increase in thickness did not lead to increase in  $J_{sc}$ , but to a decrement in present work. This suggests that charge recombination process dominated the variation of  $J_{sc}$  with respect to thickness. It is believed that the probability of photogenerated electrons and holes to transport to ZnO NRAs and Ag, respectively, became higher with thinner photoactive layer. The  $R_s$  decreased significantly from  $397.24 \pm 30.87$  to  $25.40 \pm 6.91$   $\Omega$  cm<sup>2</sup> and from  $220.26 \pm 11.53$  to  $15.97 \pm 2.47$   $\Omega$  cm<sup>2</sup> as the polymer solution concentration reduced for CB and CF devices, respectively. This result indicates the decrease of bulk resistance across the organic photoactive layer with decreasing thickness, leading to higher number of electron and hole extracted from the device. Besides, the increase of  $V_{oc}$  with the solution concentration for both solvents could be due to suppression of leakage current as indicated by larger  $R_{sh}$ . The significant decrement of  $R_s$  with respect to  $R_{sh}$  leads to increment in FF. Therefore, the increase in both  $J_{sc}$  and FF was great enough to offset the reduced  $V_{oc}$ , which in turn improved the overall device performance. The overall photovoltaic performance of all devices is summarized in Table 1.

Figure 4 shows IPCE spectra of the devices measured from wavelength 350 to 800 nm with maximum IPCE of

~16% and ~20% at 500 nm was achieved at respective lowest solution concentration for CB and CF device. Despite the increase of absorption with solution concentration, the opposite trend was observed from IPCE spectra. The IPCE result is consistent with  $J_{sc}$  which increased with decreasing solution concentration and further confirms that relatively thick organic photoactive layer on top of Eosin-Y-coated ZnO NRAs causes the increase of charge recombination in the organic photoactive layer and results in lower  $J_{sc}$  even though the absorption increased. The IPCE spectra of the CB and CF devices with the highest solution concentration exhibited low photon conversion efficiency at wavelength (500 nm) corresponding to absorption peak of MEH-PPV. For thicker photoactive layer deposited at high solution concentration, most of the photons with wavelength close to 500 nm were absorbed in the region close to FTO/Eosin-Y-coated ZnO NRAs. Meanwhile, photons with wavelength away from 500 nm were more uniformly absorbed throughout the photoactive layer. The distortion of IPCE spectrum of thick photoactive layer indicates that photocurrent generation in the bulk region close to Ag was more efficient than that in the region close to ZnO NRAs [36]. This result also suggests that the probability of holes generated in the region close to ZnO NRAs to be trapped or recombine before reaching Ag was higher.

Figure 5 shows the topographic images of surface morphology of organic photoactive layer deposited on Eosin-Y-coated ZnO NRAs with different solvent concentrations. The root mean square (rms) roughness significantly increased from 2.58 to 14.75 nm and from 4.11 to 17.77 nm, respectively, as the CB and CF solution concentration decreased. The rough surface obtained from lower solution concentration indicates ZnO NRAs were not fully covered by polymer

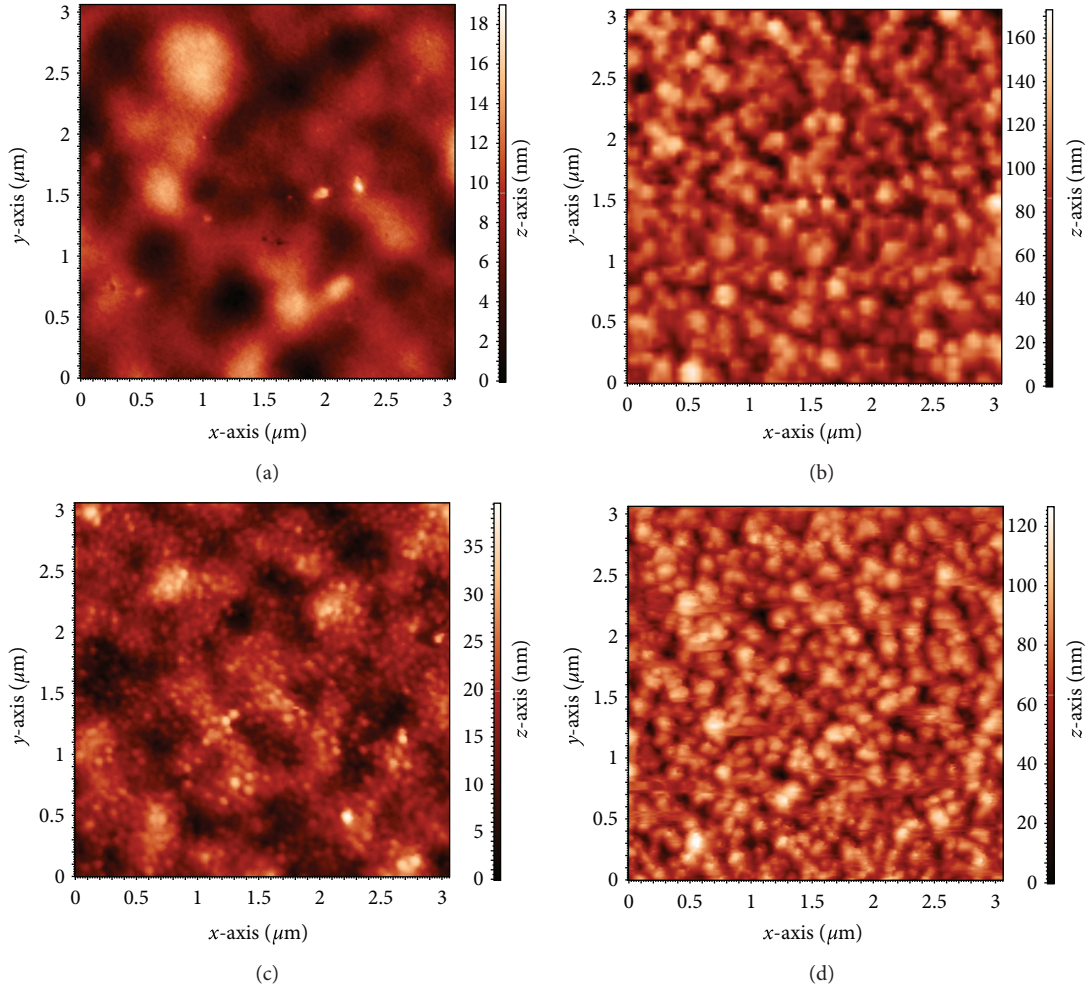


FIGURE 5: AFM images of blend films of Eosin-Y-coated ZnO NRAs and organic photoactive layer prepared from CB at concentrations (a) 10 mg/mL, (b) 6 mg/mL and prepared from CF at concentrations (c) 8 mg/mL, (d) 4 mg/mL.

TABLE 1: Summary of photovoltaic parameters of devices at various solution concentrations.

Concentration (mg/mL)	$J_{sc}$ ( $\text{mA cm}^{-2}$ )	$V_{oc}$ (V)	PCE (%)	FF	$R_s$ ( $\Omega \text{ cm}^2$ )	$R_{sh}$ ( $\Omega \text{ cm}^2$ )
Chlorobenzene						
10	$1.06 \pm 0.07$	$0.53 \pm 0.03$	$0.17 \pm 0.03$	$0.29 \pm 0.01$	$397.24 \pm 30.87$	$618.54 \pm 30.87$
8	$1.77 \pm 0.08$	$0.50 \pm 0.03$	$0.29 \pm 0.04$	$0.31 \pm 0.02$	$188.80 \pm 30.88$	$402.77 \pm 52.21$
6	$3.45 \pm 0.17$	$0.34 \pm 0.02$	$0.54 \pm 0.10$	$0.48 \pm 0.02$	$25.40 \pm 6.91$	$340.56 \pm 11.07$
Chloroform						
8	$1.51 \pm 0.07$	$0.50 \pm 0.03$	$0.24 \pm 0.03$	$0.32 \pm 0.01$	$220.26 \pm 11.53$	$526.98 \pm 46.07$
6	$2.84 \pm 0.13$	$0.49 \pm 0.04$	$0.55 \pm 0.08$	$0.41 \pm 0.01$	$51.75 \pm 6.70$	$322.64 \pm 53.53$
4	$4.76 \pm 0.17$	$0.35 \pm 0.03$	$0.87 \pm 0.15$	$0.51 \pm 0.02$	$15.97 \pm 2.47$	$272.05 \pm 35.96$

blend. This finding is in agreement with the value of  $R_{sh}$  which increased with solution concentration. Besides, this observation is also well in line with the cross-sectional FESEM images from which a wavy surface reflecting the ZnO NRAs underneath was clearly observed when organic

photoactive layer was deposited from a low solution concentration. Meanwhile, the rougher surface also provides larger contact area between organic photoactive layer and metal contact, and thus leading to better charge collection efficiency [37, 38]. Even though better photovoltaic performance can

be achieved by depositing a thinner organic photoactive film, the film must be thick enough to prevent the direct leakage current from ZnO NRAs to Ag electrode.

#### 4. Conclusions

The effect of solution concentration of MEH-PPV and PCBM deposited onto Eosin-Y-coated ZnO NRAs on the performance of inverted-type organic solar cell has been investigated. The short circuit current density and power conversion efficiency greatly enhanced with decrease of solution concentration for both chlorobenzene- and chloroform-based devices, mainly due to reduce of charge recombination in thinner organic photoactive layer and larger contact area between the rougher organic photoactive layer and Ag contact. In contrast, the increase of leakage current from ZnO NRAs to Ag at lower solution concentration results in decrease of open circuit voltage. The highest power conversion efficiencies of  $0.54 \pm 0.10\%$  and  $0.87 \pm 0.15\%$  were achieved at the respective lowest solution concentration of CB and CF. It has been shown that the solution concentration played important role in improving performance of inverted-type organic solar cell.

#### Acknowledgments

This work has been carried out with the financial support of Malaysian Ministry of Science, Technology and Innovation (MOSTI) under Science Fund 03-01-02-SF0725. The authors would like to thank Mr. Idris Zulkifle from School of Applied Physics, Universiti Kebangsaan Malaysia for silver sputtering. The authors would also like to acknowledge Mr. Mohamad Hasnul Naim Abd Hamid and Mr. Muhammad Nazrul Zahari, both from Centre Research and Instrumentation Management (CRIM), Universiti Kebangsaan Malaysia, for FESEM and AFM characterizations, respectively.

#### References

- [1] G. Li, R. Zhu, and Y. Yang, "Polymer solar cells," *Nature Photonics*, vol. 6, pp. 153–161, 2012.
- [2] G. Yu, J. Gao, J. C. Hummelen, F. Wudl, and A. J. Heeger, "Polymer photovoltaic cells: enhanced efficiencies via a network of internal donor-acceptor heterojunctions," *Science*, vol. 270, no. 5243, pp. 1789–1791, 1995.
- [3] J. Y. Kim, K. Lee, N. E. Coates et al., "Efficient tandem polymer solar cells fabricated by all-solution processing," *Science*, vol. 317, no. 5835, pp. 222–225, 2007.
- [4] W. H. Kim, A. J. Mäkinen, N. Nikolov, R. Shashidhar, H. Kim, and Z. H. Kafafi, "Molecular organic light-emitting diodes using highly conducting polymers as anodes," *Applied Physics Letters*, vol. 80, no. 20, pp. 3844–3846, 2002.
- [5] M. P. de Jong, L. J. van Ijzendoorn, and M. J. A. de Voigt, "Stability of the interface between indium-tin-oxide and poly(3,4-ethylenedioxythiophene)/poly(styrenesulfonate) in polymer light-emitting diodes," *Applied Physics Letters*, vol. 77, no. 14, pp. 2255–2257, 2000.
- [6] M. Jørgensen, K. Norrman, and F. C. Krebs, "Stability/degradation of polymer solar cells," *Solar Energy Materials and Solar Cells*, vol. 92, no. 7, pp. 686–714, 2008.
- [7] F. Zhang, X. Xu, W. Tang et al., "Recent development of the inverted configuration organic solar cells," *Solar Energy Materials and Solar Cells*, vol. 95, no. 7, pp. 1785–1799, 2011.
- [8] Y. Sun, J. H. Seo, C. J. Takacs, J. Seifert, and A. J. Heeger, "Inverted polymer solar cells integrated with a low-temperature-annealed sol-gel-derived ZnO film as an electron transport layer," *Advanced Materials*, vol. 23, no. 14, pp. 1679–1683, 2011.
- [9] A. K. K. Kyaw, X. W. Sun, C. Y. Jiang, G. Q. Lo, D. W. Zhao, and D. L. Kwong, "An inverted organic solar cell employing a sol-gel derived ZnO electron selective layer and thermal evaporated MoO<sub>3</sub> hole selective layer," *Applied Physics Letters*, vol. 93, no. 22, Article ID 221107, 3 pages, 2008.
- [10] S. K. Hau, H. L. Yip, N. S. Baek, J. Zou, K. O'Malley, and A. K. Y. Jen, "Air-stable inverted flexible polymer solar cells using zinc oxide nanoparticles as an electron selective layer," *Applied Physics Letters*, vol. 92, no. 25, Article ID 253301, 3 pages, 2008.
- [11] D. C. Lim, W. H. Shim, K. D. Kim et al., "Spontaneous formation of nanoripples on the surface of ZnO thin films as hole-blocking layer of inverted organic solar cells," *Solar Energy Materials and Solar Cells*, vol. 95, no. 11, pp. 3036–3040, 2011.
- [12] S. R. Ferreira, R. J. Davis, Y. J. Lee, P. Lu, and J. W. P. Hsu, "Effect of device architecture on hybrid zinc oxide nanoparticle:poly(3-hexylthiophene) blend solar cell performance and stability," *Organic Electronics*, vol. 12, no. 7, pp. 1258–1263, 2011.
- [13] M. Y. Lin, C. Y. Lee, S. C. Shiu et al., "Sol-gel processed CuOx thin film as an anode interlayer for inverted polymer solar cells," *Organic Electronics*, vol. 11, no. 11, pp. 1828–1834, 2010.
- [14] N. Sekine, C. H. Chou, W. L. Kwan, and Y. Yang, "ZnO nanoridge structure and its application in inverted polymer solar cell," *Organic Electronics*, vol. 10, no. 8, pp. 1473–1477, 2009.
- [15] M. N. Shan, S. S. Wang, Z. Q. Bian, J. P. Liu, and Y. L. Zhao, "Hybrid inverted organic photovoltaic cells based on nanoporous TiO<sub>2</sub> films and organic small molecules," *Solar Energy Materials and Solar Cells*, vol. 93, no. 9, pp. 1613–1617, 2009.
- [16] R. Steim, S. A. Choulis, P. Schilinsky, and C. J. Brabec, "Interface modification for highly efficient organic photovoltaics," *Applied Physics Letters*, vol. 92, no. 9, Article ID 093303, 3 pages, 2008.
- [17] T. Kuwabara, T. Nakayama, K. Uozumi, T. Yamaguchi, and K. Takahashi, "Highly durable inverted-type organic solar cell using amorphous titanium oxide as electron collection electrode inserted between ITO and organic layer," *Solar Energy Materials and Solar Cells*, vol. 92, no. 11, pp. 1476–1482, 2008.
- [18] C. Waldauf, M. Morana, P. Denk et al., "Highly efficient inverted organic photovoltaics using solution based titanium oxide as electron selective contact," *Applied Physics Letters*, vol. 89, no. 23, Article ID 233517, 3 pages, 2006.
- [19] G. D. Sharma, J. A. Mikroyannidis, and S. P. Singh, "Efficient bulk heterojunction solar cells based on D-A copolymers as electron donors and PC70BM as electron acceptor," *Materials Chemistry and Physics*, vol. 135, no. 1, pp. 25–31, 2012.
- [20] H. H. Liao, L. M. Chen, Z. Xu, G. Li, and Y. Yang, "Highly efficient inverted polymer solar cell by low temperature annealing of Cs<sub>2</sub>CO<sub>3</sub> interlayer," *Applied Physics Letters*, vol. 92, no. 17, Article ID 173303, 3 pages, 2008.
- [21] Z. Q. Xu, J. P. Yang, F. Z. Sun, S. T. Lee, Y. Q. Li, and J. X. Tang, "Efficient inverted polymer solar cells incorporating doped organic electron transporting layer," *Organic Electronics*, vol. 13, no. 4, pp. 697–704, 2012.
- [22] M. Lira-Cantu and F. C. Krebs, "Hybrid solar cells based on MEH-PPV and thin film semiconductor oxides (TiO<sub>2</sub>, Nb<sub>2</sub>O<sub>5</sub>,

- ZnO, CeO<sub>2</sub> and CeO<sub>2</sub>-TiO<sub>2</sub>): performance improvement during long-time irradiation,” *Solar Energy Materials and Solar Cells*, vol. 90, no. 14, pp. 2076–2086, 2006.
- [23] S. Han, W. S. Shin, M. Seo, D. Gupta, S. J. Moon, and S. Yoo, “Improving performance of organic solar cells using amorphous tungsten oxides as an interfacial buffer layer on transparent anodes,” *Organic Electronics*, vol. 10, no. 5, pp. 791–797, 2009.
- [24] L. Vayssieres, “Growth of arrayed nanorods and nanowires of ZnO from aqueous solutions,” *Advanced Materials*, vol. 15, no. 5, pp. 464–466, 2003.
- [25] K. Takanezawa, K. Hirota, Q. S. Wei, K. Tajima, and K. Hashimoto, “Efficient charge collection with ZnO nanorod array in hybrid photovoltaic devices,” *Journal of Physical Chemistry C*, vol. 111, no. 19, pp. 7218–7223, 2007.
- [26] C. Y. Chou, J. S. Huang, C. H. Wu, C. Y. Lee, and C. F. Lin, “Lengthening the polymer solidification time to improve the performance of polymer/ZnO nanorod hybrid solar cells,” *Solar Energy Materials and Solar Cells*, vol. 93, no. 9, pp. 1608–1612, 2009.
- [27] B. K. Crone, I. H. Campbell, P. S. Davids, and D. L. Smith, “Charge injection and transport in single-layer organic light-emitting diodes,” *Applied Physics Letters*, vol. 73, no. 21, pp. 3162–3164, 1998.
- [28] W. J. Lee, H. Okada, A. Wakahara, and A. Yoshida, “Structural and photoelectrochemical characteristics of nanocrystalline ZnO electrode with Eosin-Y,” *Ceramics International*, vol. 32, no. 5, pp. 495–498, 2006.
- [29] M. S. White, D. C. Olson, S. E. Shaheen, N. Kopidakis, and D. S. Ginley, “Inverted bulk-heterojunction organic photovoltaic device using a solution-derived ZnO underlayer,” *Applied Physics Letters*, vol. 89, no. 14, Article ID 143517, 3 pages, 2006.
- [30] H. Kim, J. Y. Kim, K. Lee, Y. Park, Y. Jin, and H. Suh, “Organic photovoltaic cells based on conjugated polymer/fullerene composites,” *Current Applied Physics*, vol. 1, no. 2-3, pp. 139–143, 2001.
- [31] C. T. Chen, F. C. Hsu, S. W. Kuan, and Y. F. Chen, “The effect of C60 on the ZnO-nanorod surface in organo-inorganic hybrid photovoltaics,” *Solar Energy Materials and Solar Cells*, vol. 95, no. 2, pp. 740–744, 2011.
- [32] G. Li, V. Shrotriya, Y. Yao, J. Huang, and Y. Yang, “Manipulating regioregular poly(3-hexylthiophene): [6,6]-phenyl-C 61-butyric acid methyl ester blends—route towards high efficiency polymer solar cells,” *Journal of Materials Chemistry*, vol. 17, no. 30, pp. 3126–3140, 2007.
- [33] P. H. Chen, H. H. Chen, R. Anbarasan, and L. S. Kuo, “Synthesis and characterization of Eosin Y functionalized MWCNT,” in *Proceedings of the 4th IEEE Nanotechnology Materials and Devices Conference (NMDC '10)*, pp. 325–327, Monterey, Calif, USA, October 2010.
- [34] D. Bi, F. Wu, Q. Qu et al., “Device performance related to amphiphilic modification at charge separation interface in hybrid solar cells with vertically aligned ZnO nanorod arrays,” *Journal of Physical Chemistry C*, vol. 115, no. 9, pp. 3745–3752, 2011.
- [35] D. C. Olson, Y. J. Lee, M. S. White et al., “Effect of polymer processing on the performance of poly(3-hexylthiophene)/ZnO nanorod photovoltaic devices,” *Journal of Physical Chemistry C*, vol. 111, no. 44, pp. 16640–16645, 2007.
- [36] J. K. B. Thomas, V. Yana, L. Zhe, K. Dinesh, H. F. Richard, and R. M. Christopher, “White-light bias external quantum efficiency measurements of standard and inverted P3HT:PCBM photovoltaic cells,” *Journal of Physics D*, vol. 45, no. 41, Article ID 415101, 2012.
- [37] T. W. Lee and O. O. Park, “The effect of different heat treatments on the luminescence efficiency of polymer light-emitting diodes,” *Advanced Materials*, vol. 12, no. 11, pp. 801–804, 2000.
- [38] Y. M. Shen, C. S. Chen, P. C. Yang, S. Y. Ma, and C. F. Lin, “Improvement of surface morphology of thin films and performance by applying electric field on P3HT:PCBM based solar cells,” *Solar Energy Materials and Solar Cells*, vol. 99, pp. 263–267, 2012.